RESEARCH ARTICLE



Mesenchymal stromal/stem cell tissue source and in vitro expansion impact extracellular vesicle protein and miRNA compositions as well as angiogenic and immunomodulatory capacities

Christina Holmes¹

²Department of Biomedical Sciences, College of Medicine, Florida State University, Tallahassee, Florida, USA

Correspondence

Christina Holmes, 2525 Pottsdamer St., Tallahassee, FL 32310, USA. Email: christinaa.holmes@gmail.com

Funding information

National Institutes of Health, Grant/Award Numbers: R01NS125016, R16GM151369

Abstract

Recently, therapies utilizing extracellular vesicles (EVs) derived from mesenchymal stromal/stem cells (MSCs) have begun to show promise in clinical trials. However, EV therapeutic potential varies with MSC tissue source and in vitro expansion through passaging. To find the optimal MSC source for clinically translatable EV-derived therapies, this study aims to compare the angiogenic and immunomodulatory potentials and the protein and miRNA cargo compositions of EVs isolated from the two most common clinical sources of adult MSCs, bone marrow and adipose tissue, across different passage numbers. Primary bone marrow-derived MSCs (BMSCs) and adipose-derived MSCs (ASCs) were isolated from adult female Lewis rats and expanded in vitro to the indicated passage numbers (P2, P4, and P8). EVs were isolated from the culture medium of P2, P4, and P8 BMSCs and ASCs and characterized for EV size, number, surface markers, protein content, and morphology. EVs isolated from different tissue sources showed different EV yields per cell, EV sizes, and protein yield per EV. Gene ontology (GO) and Kyoto Encyclopedia of Genes and Genomes (KEGG) pathway analyses of proteomics data and miRNA seq data identified key proteins and pathways associated with differences between BMSC-EVs and ASC-EVs, as well as differences due to passage number. In vitro tube formation assays employing human umbilical vein endothelial cells suggested that both tissue source and passage number had significant effects on the angiogenic capacity of EVs. With or without lipopolysaccharide (LPS) stimulation, EVs more significantly impacted expression of M2-macrophage genes (IL-10, Argl, TGFβ) than M1-macrophage genes (IL-6, NOS2, TNF α). By correlating the proteomics analyses with the miRNA seq analysis and differences observed in our in vitro immunomodulatory, angiogenic, and proliferation assays, this study highlights the trade-offs that may be necessary in selecting the optimal MSC source for development of clinical EV therapies.

KEYWORDS

angiogenesis, extracellular vesicles, immunomodulation, in vitro aging, mesenchymal stem/stromal cells, multi-omics, tissue of origin

This is an open access article under the terms of the Creative Commons Attribution-NonCommercial License, which permits use, distribution and reproduction in any medium, provided the original work is properly cited and is not used for commercial purposes.

© 2024 The Author(s). Journal of Extracellular Vesicles published by Wiley Periodicals LLC on behalf of International Society for Extracellular Vesicles.

¹Department of Chemical & Biomedical Engineering, Florida A&M University-Florida State University College of Engineering, Florida State University, Tallahassee, Florida, USA

1 | INTRODUCTION

Mesenchymal stromal/stem cells (MSCs) have demonstrated tremendous potential in regenerative medicine and cell-based therapies (Liu & Holmes, 2021). Despite the significant progress made by MSCs in clinical trials, such as in the treatment of osteoarthritis (Matas et al., 2019), systemic lupus erythematosus (Zhang et al., 2019), amyotrophic lateral sclerosis, spinal cord injury, graft-vs-host disease (Kadri et al., 2023), diabetes mellitus (Huang et al., 2021), myocardial infarction (Dong et al., 2012), ischemic stroke (Gong et al., 2021) and chronic wounds (Guillamat-Prats, 2021), there has been growing interest in therapeutic MSC-derived extracellular vesicles (EVs) due to their advantages over MSC transplantation therapies. EVs are cell-secreted nano size membrane-encapsulated particles that consist of proteins, nucleic acids, and lipids and play crucial roles in cell-cell communication and modulation of physiological processes, including immunoregulation and tissue regeneration and repair (Nagelkerke et al., 2021). Demonstrating natural biocompatibility, inherent long-circulation ability in vivo, limited immunogenicity, low cytotoxicity, easy transport through physiological barriers, and the potential for specific targeting, EVs have emerged as a promising therapeutic option for treating various diseases (Maumus et al., 2013). To date, EVs derived from a range of MSC tissue sources have exhibited significant therapeutic benefits in multiple preclinical disease models, including acute liver injury (Lin et al., 2022), spinal cord injury (Liu et al., 2020), and bone healing (Zou et al., 2023). Meanwhile, clinical studies employing EVs from various MSC sources have successfully demonstrated safety and efficacy in the treatment of SARS-CoV-2 related pneumonia (NCT04313647, NCT04276987) (Shi et al., 2021; Zhu et al., 2022), malignant middle cerebral artery infarcts (NCT03384433) (Dehghani et al., 2022), and knee osteoarthritis (NCT02580695) (Matas et al., 2024). Further clinical studies are also actively assessing MSC-EVs for the treatment of premature ovarian failure (NCT06202547), as a topical ointment for the treatment of psoriasis (NCT05523011), and for skin rejuvenation applications (NCT05813379). While the full extent of their biological and therapeutic properties is currently under investigation, MSC-EVs are a promising alternative and/or addition to current cell

Although MSCs can be isolated from a wide variety of tissue sources, including umbilical cord blood, Wharton's jelly, placenta, skeletal muscle, dental pulp, skin, and menstrual blood (Fernández-Santos et al., 2022), bone marrow and adipose tissue are the most widely used adult clinical MSC sources as they can be employed in both autologous and allogenic therapies. Bone marrow-derived mesenchymal stem cells (BMSCs) have been extensively studied, providing many of the foundational observations of MSC biology and therapeutic applications. However, the invasive procedure to obtain bone marrow and the decreasing frequency and differentiation potential of BMSCs with donor age have led researchers to explore alternative sources (Bagge et al., 2022). Adipose-derived MSCs (ASCs), by contrast, are easily accessed and obtained due to their higher frequency in adipose tissue, making them an attractive alternative source for MSCs. While EVs derived from BMSCs, ASCs, umbilical cord MSCs (UMSCs), MSCs obtained from human induced pluripotent stem cells (iMSCs), and other MSC sources have demonstrated therapeutic efficacy in various pre-clinical models, such as osteoarthritis (Zhu et al., 2017), ischemic disease (Bian et al., 2014), and GVHD (Wang et al., 2016), in the few direct comparison studies to date, they have shown both similarities and noteworthy distinctions. For example, Hoang et al. found that BMSC-EVs were superior in stimulating dermal fibroblast proliferation compared to ASC-EVs, while ASC-EVs led to increased keratinocyte proliferation (Hoang et al., 2020). Similarly, ASC-EVs promoted greater angiogenic tube formation and resulted in a significantly higher wound closure rate in a murine diabetic wound model, while BMSC-EVs induced enhanced proliferation in keratinocytes and endothelial cells and superior viability in fibroblasts (Pomatto et al., 2021). In a cardioprotection study, ASC-EVs significantly improved cardiac function by the inhibition of cardiomyocyte apoptosis and enhanced angiogenesis compared to BMSC-EVs and UMSC-EVs (Xu et al., 2020). Although these initial comparison studies of EV efficacy across MSC sources have provided some insights, the MSCs used in these studies were varied in donor species, passage number, cryopreservation details, and donor health status, leaving an incomplete picture of the potential therapeutic advantages of one source over another. Thus, determining the appropriate MSC tissue source to produce EVs with maximal therapeutic potential for a specific clinical application remains a critical challenge to clinical translation.

In addition to differences due to tissue origin, MSCs exhibit varying properties based on donor profiles, their exposure to in vitro aging, and changes in culture conditions. Initial studies suggest that MSC-EVs can also be influenced by these factors. For example, TNF α -primed MSCs secreted EVs containing elevated levels of Galectin-1 and promoted M2 macrophage polarization in a murine intrauterine adhesion model (Li et al., 2022). Similarly, Shin et al. showed that priming MSCs with α -synuclein enhanced expression of autophagy-associated miRNAs in MSC-EVs and decreased neurodegeneration in murine parkinsonian models (Shin et al., 2022). However, deciphering how these variations in conditions impact MSC-EV properties is challenging. Due to the low abundance of MSCs in tissues, in vitro expansion of MSCs is essential for obtaining the large numbers of cells needed for clinical applications. However, the process of in vitro cellular aging has been recently shown to diminish the therapeutic efficacy of EVs in vivo and in vitro. For example, Kim et al. demonstrated that the immunomodulatory effectiveness of EVs derived from MSCs obtained from human induced pluripotent stem cells (iMSCs) was reduced following in vitro expansion. This decrease in therapeutic capacity was observed in a mouse model of primary Sjögren's syndrome and was associated with related changes in EV microRNA and protein content (Kim et al., 2021). While in vitro expansion is recognized to influence the

properties of MSCs, the precise effects on the quality, quantity, and therapeutic potential of the EVs they secrete have yet to be fully elucidated.

Although several studies have evaluated the properties of EVs secreted by MSCs under different conditions, it remains unclear how specific tissue sources and in vitro aging contribute to distinct EV cargo profiles and how that might impact EV clinical efficacy in various applications. To address these gaps, this study conducted a comprehensive characterization and comparison of EVs derived from the two most widely employed clinical MSC types, ASCs and BMSCs, at several passage numbers, including small RNA sequencing and proteomics analyses of EV cargo. These comparative EV profiling results were accompanied by in vitro angiogenic and immunomodulatory functional assays, since the majority of clinical MSC and MSC-EV therapies typically target diseases and conditions where vascularization and immune responses are of key importance. In this study, BMSCs and ASCs were isolated from the same donor rats of the inbred Lewis strain to minimize genetic variability and maintain consistent environmental and historical exposures. By doing so, this study provides insight into the underlying cargos and mechanisms that contribute to similarities and differences in EV angiogenic and immunomodulatory capacities and investigates key EV properties that are altered during in vitro expansion. Thus, this research significantly contributes to the development of clinical MSC-EV therapies by highlighting the trade-offs that may be necessary between specific therapeutic potentials and/or driving higher EV yield when selecting an optimal MSC source for large-scale EV production for specific clinical applications.

2 | MATERIAL AND METHODS

2.1 | Primary bone marrow- and adipose- derived MSC isolation and culture

The following study was approved by the Institutional Animal Care and Use Committee at Florida State University (202000070). Female 4–6-month-old Lewis rats were purchased from Charles River Laboratories. Each batch of isolated primary cells was pooled from three rats. Bone marrow MSCs (BMSCs) were isolated from bilateral femurs and tibias via flushing as previously described (Gudleviciene et al., 2015). Abdominal subcutaneous fat pads were isolated, minced, and digested with Collagenase Type I (Gibco, 17100017) at 37°C for derivation of adipose-derived MSCs (ASCs) as previously described (Raposio et al., 2017). Both cell types were treated with red blood cell (RBC) lysis buffer (eBioscience, 00433357) and filtered through a 100 μ m cell strainer (VWR, 76327102) prior to seeding and culture in high glucose Dulbecco's Modified Eagle Medium (DMEM) (Gibco, 11995065) supplemented with 10% Fetal Bovine Serum (FBS) (VWR, 89510186) and 1% Penicillin-Streptomycin (Pen Strep) (Gibco, 15140148) in a humidified incubator maintaining 5% CO₂ at 37°C (Gudleviciene et al., 2015). For both cell types, media were changed every 3 days. When adherent cells became 80%–90% confluent, MSCs were washed with phosphate buffered saline (PBS) (Gibco, 14190250), treated with 0.25% trypsin-EDTA (Gibco, 25200056), counted, and reseeded at a split ratio of 1:4. MSCs were defined as Passage 0 (P0) from the time of isolation to the stage where an initial confluent monolayer was formed. Every instance of trypsinization and reseeding increased the MSC passage number by a count of one. MSCs were expanded in culture until the indicated number, up to passage 8 (P8).

2.2 | Flow cytometry analysis of MSC phenotype

Cells were harvested from culture flasks via trypsinization, washed with PBS, and resuspended at a concentration of 1×10^6 cells/mL in staining buffer: ice cold PBS containing 0.5% (wt./vl.) bovine serum albumin (BSA). To block Fc receptors, $100~\mu$ L of cell solution was mixed with $100~\mu$ L of 5% (vl./vl.) rat serum (Sigma, R9759) in staining buffer, incubated on ice for 20 min, and subsequently centrifuged at 1500 rpm for 5 min at 4°C. Supernatant was discarded and $100~\mu$ L of either staining buffer or buffer containing one or more of the following antibodies at the indicated dilution factor(s) was added: FITC antimouse/rat CD29 (HM β 1-1) (1:400), PE anti-rat CD90/mouse CD90 (OX-7) (1:500), PE/Cyanine7 anti-rat CD45 (OX-1) (1:500), and PerCP/Cyanine5.5 anti-rat CD11b/c (OX-42) (1:500) (Biolegend, CA, USA). Cell solutions were incubated for 30 min on ice in the dark, washed three times, resuspended in $400~\mu$ L of staining buffer, and subsequently filtered through a 52 μ m strainer mesh (Component Supply, U-CMN-52). Surface staining quantification was performed on a BD FACSCanto Flow Cytometer (BD, Franklin Lakes, NJ, USA) and the data were analysed via FACSDiva software against isotype controls.

2.3 | EV isolation by extraPEG-based ultracentrifugation

Exosome-depleted FBS was produced by ultracentrifugation (UC) of FBS at 29,000 rpm in a SW32 rotor for 20 h at 4°C. After MSCs reached 80% confluency, culture media was changed completely to media containing exosome-depleted FBS. Conditioned culture media (CCM) was then collected after 72 h. Differential UC combined with polyethylene glycol (PEG) (Sigma-Aldrich, 81260) precipitation was performed to isolate EVs from CCM as previously described (Rider et al., 2016). Briefly, CCM underwent

sequential centrifugation as follows, with the supernatant retained from each round: 500 g for 5 min, 2000 g for 10 min, and 10,000 g for 30 min. Next, PEG solution (16% wt./vol., 1.0 M NaCl) was added to the supernatant to a final concentration of 8% PEG and incubated at 4°C for 12–16 h. The solution was subsequently centrifuged at 3214 g for 1 h in a TX-400 rotor (Thermo Scientific, 75003181) in the Heraeus Multifuge X1R centrifuge (Thermo Scientific, Waltham, MA, US) and the resulting pellet was resuspended in $0.2 \,\mu$ m-filtered sterile PBS. Finally, after UC at 110,000 g for 70 min in an open-top thickwall polypropylene tube (Beckman Coulter, 347287) in the Optima MAX-XP Ultracentrifuge (Beckman Coulter, Brea, CA, USA) using the TLA120.2 rotor, the resulting EV pellet was dissolved in $0.2 \,\mu$ m-filtered sterile PBS. All centrifugation steps were conducted at 4°C.

2.4 | Nanoparticle tracking analysis (NTA) of EVs

EV samples were diluted in fresh MilliQ water to a concentration of 0.2–1.8×10⁹ EVs/mL and injected into a NanoSight LM10-HS instrument (Malvern Instruments, Malvern, UK). Analysis of particle concentration, size distribution, mean size, and mode size was performed using NanoSight Software version 3.4 with a camera level of 13, a video time of 60 s, and a detection threshold of 5. Each EV sample was repeatedly injected and measured three times. Between each sample injection, the instrument chamber was cleaned with fresh MilliQ water and air in sequence.

2.5 | EV protein quantification

To lyse EV samples for protein quantification, 3 μ L of 10% sodium dodecyl sulfate (SDS) solution was mixed with 27 uL of EV sample solution and was incubated for 1 min at room temperature (RT). The total protein content of 25 μ L of the resulting solution was measured via the Pierce BCA Protein Assay (Thermo Scientific, 23225) according to manufacturer's instructions.

2.6 Western blotting analysis of EV markers

To analyse EV expression of protein markers, 20 μ g EV samples were lysed in 1% SDS solution on ice for 30 min with occasional vortexing. After centrifugation at 20,000 g for 10 min at 4°C, the supernatant was kept for further analysis. Protein samples were mixed with 5× loading buffer and boiled at 95°C for 10 min. Samples were loaded into precast 10% Bis-Tris gels, separated by SDS-PAGE, and transferred onto a nitrocellulose membrane (Amersham Protran 0.45 μ M NC, 10600002), with transfer results confirmed by Ponceau S staining. Membranes were blocked with 5% non-fat milk at RT for 1 h. Antibody solutions were prepared at the indicated dilutions in 2.5% bovine serum albumin (BSA) in Tris-buffered saline (10 mM Tris-HCl and 150 mM NaCl) with 0.1% Tween 20 (vl./vl.) (TBST) as follows: Calnexin (Santa Cruz, sc-11397, 1:1000), GAPDH (GeneTex, GTX-100118, 1:5000), HSC70 (Santa Cruz, sc-7298, 1:1000), CD63 (GeneTex, GTX17441, 1:500), CD9 (Bioss, bs-2489R, 1:500), TSG101 (Santa Cruz, sc-7964, 1:1000). Membranes were incubated in primary antibody solutions at 4°C overnight under gentle rocking (20 rpm). Membranes were washed three times for 5 min in TBST, followed by incubation with secondary antibody solution for 45 min at RT. Membrane washing was repeated three times and an equal volume of radiance peroxide (Azure biosystems, S1003) and either radiance substrate (Azure biosystems, S1001) or radiance plus substrate (Azure biosystems, S1005) were mixed and applied to the membrane gently. The membrane was then quickly imaged via the ChemiDoc Imaging System (Bio-Rad, Hercules, CA, USA).

2.7 | Transmission electron microscopy (TEM) of EVs

TEM was performed as previously described to confirm EV morphology (Lässer et al., 2012). Briefly, 10 μ L of EV solution at a particle concentration of 1×10⁹/mL was dropped onto parafilm. A carbon support film hexagonal 400 mesh copper grid (Electron Microscopy Sciences, CF400H-CU) was placed on top of the EV solution drop for 1 h at room temperature (RT) with the coated side down. The grid was then washed with sterile filtered PBS three times by moving the grid from one drop of 30 μ L PBS to another. To avoid disrupting the attached EVs on the grid surface, grids were gently touched to absorbance paper to remove excess solution between drops. A 20 μ L drop of 2% paraformaldehyde (Electron Microscopy Sciences, EM Grade) was subsequently used to fix EVs on the surface of the grid for 10 min at RT, followed by a wash step using MilliQ water, and incubation with a 20 μ L drop of 2.5% glutaraldehyde (Electron Microscopy Sciences, EM Grade) for another 10 min at RT. After another MilliQ water wash step, the grid was placed on a 20 μ L drop of 2% uranyl acetate (Electron Microscopy Sciences) and then transferred to a 20 μ L drop of 0.1% methyl cellulose and 0.4% uranyl acetate and incubated for a further 10 min at RT. Finally, excess solution was removed with absorbance paper and the grid was flipped over to dry for imaging via a HT7800 RuliTEM (Hitachi, Tokyo, Japan).



2.8 | Proteomics analysis of EV protein cargo via liquid chromatography-mass spectrometry (LC-MS/MS)

Five biological replicates were analysed for each passage number and EV tissue source. Proteins were isolated and digested using S-Trap micro columns (\leq 100 μ g) (ProtiFi, C02-micro-40) according to the manufacturer protocol. Briefly, 10 μ g of EV sample was digested using Trypsin (Promega, V5111) and ProteaseMAX Surfactant Trypsin Enhancer (Promega, V2071) and the resulting column elution was dried in a SpeedVac Concentrator (Thermo Scientific Savant, SPD111V). The dried peptides were subsequently resuspended using the Pierce High pH Reversed-Phase Peptide Fractionation Kit (Thermo Scientific, 84868). Briefly, three fractions were obtained from the kit and the resulting elutions were separately dried in a SpeedVac Concentrator and submitted to the Florida State University Translational Laboratory. An Orbitrap Exploris 480 Mass Spectrometer (ThermoFisher Scientific) was used for peptide analysis as previously described (Nimma et al., 2022). Thermo Proteome Discoverer 2.5.0.400 was used for raw data mapping using the search engines SequestHT, Mascot, and Amanda for initial analysis. STRING Version 11.5 and Cytoscape Version 3.9.1 were used for Kyoto Encyclopedia of Genes and Genomes (KEGG) and gene ontology (GO) enrichment analyses, as well as to map protein-protein interactions.

2.9 | miRNA sequencing of EVs for miRNA cargo analysis

Total RNA was isolated from EVs using a modified Trizol method as previously described (Zhao et al., 2017), with three biological replicates in each group. Resulting RNA pellets were resuspended in 6 μ L of MilliQ water and the Qubit microRNA Assay Kit (Invitrogen, Q32880) was used to quantify the microRNA within the RNA sample with a Qubit 2.0 fluorometer (Invitrogen). Subsequently, the cDNA library was constructed using the QIAseq miRNA Library Kit (QIAGEN, 331502) and the QIAseq miRNA 48 Index IL (QIAGEN, 331595) according to manufacturer protocols. The quality, quantity, and average size of the cDNA library was measured via High Sensitivity DNA ScreenTape Analysis (Agilent Technologies, 5067-4626) and the KAPA Library Quantification Kit (Kapa Biosystems, KR0405). Pooled samples were then subjected to RNA-sequencing on a NovaSeq 6000 sequencer (Illumina, San Diego, CA, USA) following the NovaSeq XP workflow running single-end 100 cycles in a SP flow lane. Raw data were uploaded to the Qiagen website according to the manual of the miRNA library kit and mapped using miRBase_v22 as reference for Rattus norvegicus (Rnor6.0.103) miRNA targets after being trimmed and filtered following workflow version 1.2. Differential expression of miRNAs was then calculated and displayed in heatmap and volcano plots with FDR < 0.5 and log2 [fold change] > 1. miRDB was used to obtain the mRNA targets of differentially expressed miRNAs (DEM). STRING Version 12.0 was then used for KEGG and GO enrichment analyses.

2.10 | Human umbilical vein endothelial cell (HUVEC) tube formation assay

HUVECs were purchased from ATCC (C2519A) and cultured in EBM-2 Basal Media (Lonza, CC-3156) supplemented with EGM-2 SingleQuots Supplements (Lonza, CC-4176). Media was changed every 48 h and cells were split at a ratio of 1:3 for each passage. Matrigel Growth Factor Reduced (GFR) Basement Membrane Matrix (Corning, 354230) was thawed and 75 µL gel/well was added to a 96-well tissue culture plate (VWR, 10062–900). Plates were incubated at RT for 10 min and subsequently placed in a humidified cell culture incubator maintaining 5% CO2 at 37°C for 30 min. BMSC-EVs or ASC-EVs derived at the indicated passage numbers were then added to individual wells at concentrations of 0, 50, and 100 µg/mL in a total volume of 75 µL of culture media, with three technical replicates for each condition, and the plates were placed in a cell culture incubator for 30 min. HUVECs were then seeded in each well at 8×10^4 cells/cm² in a 75 μ L/well volume on the top of the Matrigel and placed back into the cell culture incubator. After 16 h, media was removed, wells were washed gently twice with PBS, and phase contrast images at 4 X magnification were taken on a BioTek Cytation 5 Cell Imaging Multimode Reader (Agilent, Santa Clara, CA, USA). Images were analysed via the Angiogenesis Analyzer in ImageJ software (Carpentier et al., 2020). Tube formation parameters, specifically the number of branches, meshes, and nodes, as well as the total tube length, were extracted from the microscope images, averaged, and analysed as a measure of in vitro angiogenic capacity. EV dosages for this assay and subsequent in vitro functional assays were chosen based on previous preclinical angiogenic and immunomodulatory studies using BMSC-EVs and ASC-EVs (Liu & Holmes, 2021) and were normalized by total protein content rather than EV number to better correlate in vitro functional assay results with proteomics analysis results.

2.11 Gene expression analysis and real-time quantitative reverse transcription PCR (RT-qPCR)

RAW264.7 cells were purchased from ATCC (TIB-71). Cells were seeded (HUVECs at a density of 8×10^4 cells/cm² and RAW264.7 cells at a density of 9×10^4 cells/well) in a 96-well plate for 24 h before changing to media containing either 0, 50, or $100 \,\mu\text{g/mL}$ of BMSC-EVs or ASC-EVs derived at the indicated passage numbers for another 24 h. In the case of RAW264.7 cells, some experiments included lipopolysaccharide (LPS) treatment at a concentration of $100 \, \text{ng/mL}$ in addition to EV treatment to stimulate an immune response. After 24 h of EV treatment, RAW264.7 and HUVEC cells were washed with PBS and lysed in TRIzol reagent (Invitrogen, 15596026) for total RNA isolation according to manufacturer instructions. Reverse transcription was performed using qScript cDNA SuperMix (Quantabio, 95048–500) following manufacturer instructions. The resulting cDNA was subjected to quantitative real-time polymerase chain reaction (qRT-PCR) using PerfeCTa SYBR Green SuperMix (Quantabio, 101414-152) in a 96-well white plate (Bio-Rad, MLL9651) on a Bio-Rad CFX Connect Real-Time PCR System (Bio-Rad, Hercules, California, USA). The amplification protocol was performed as follows: 95° C for 10° C for

2.12 | RAW264.7 cell proliferation assay

RAW264.7 cells were seeded at a density of 6×10^3 cells/well in a black 96-well plate (Greiner bio-one, 655892) and treated with 100 μ g/mL of BMSC-EVs or ASC-EVs derived at the indicated passage numbers or an equal volume of PBS. Cell proliferation was measured at 15, 24, 39, 48, 63, and 72 h using the RealTime-GloTM MT Cell Viability Assay (Promega, G9711) according to manufacturer instructions on a BioTek Cytation 5 Cell Imaging Multimode Reader (Agilent, Santa Clara, CA, USA).

2.13 | BMSC and HUVEC cell proliferation assays

Cells were seeded (primary P2 BMSCs at a density of 1×10^4 cells/well and HUVECs at a density of 3×10^3 cells/well) in an E-plate 16 (Agilent, 54698300) and treated with 100 μ g/mL of BMSC-EVs or ASC-EVs derived at the indicated passage numbers or an equal volume of PBS. Cell proliferation index was measured every 30 min using the xCELLigence Real-Time Cell Analysis (RTCA) DP (dual purpose) System (Agilent, Santa Clara, CA, USA).

2.14 | Statistical analysis

All data that were statistically analysed were obtained from three or more independent experimental repeats. For each repeat, three technical replicates were pooled to calculate its mean. Where relevant, the mean of the sample means and the standard error of the sample means (SEM) were calculated, and data are expressed as mean \pm SEM. Intergroup comparisons were performed via Kruskal–Wallis tests with Dunn's multiple comparisons and two-way ANOVA test with Sidak's or Tukey's post hoc comparisons where relevant using GraphPad Prism 9.4.1. Differences were considered as statistically significant at p < 0.05 (denoted as *), very significant at p < 0.01 (denoted as **), highly significant at p < 0.001 (denoted as ***), and extremely significant at p < 0.0001 (denoted as ****).

3 | RESULTS

3.1 | Primary MSC and EV characterization

The study design is outlined in Figure 1(a). The effects of MSC tissue origin (BMSC vs. ASC) from the same animal donors and the impacts of in vitro expansion (i.e., passage number P2-P8) on MSC-EVs were investigated in this study. Flow cytometry confirmed the isolation of primary rat ASCs and BMSCs, with approximately $92.7 \pm 1.8\%$, $95.2 \pm 0.2\%$, and $91.8 \pm 2.1\%$ of ASCs and $93.0 \pm 2.5\%$, $91.2 \pm 1.9\%$, and $97.1 \pm 0.9\%$ of BMSCs displaying typical MSC surface marker expression (CD29+/CD90+/CD45-/CD11b/c-) at P2, P4, and P8, respectively (Figure 1b). BMSCs showed a more heterogeneous MSC population at P2 than the corresponding ASCs; however, MSC populations appeared less heterogeneous for each tissue source as passage number increased.

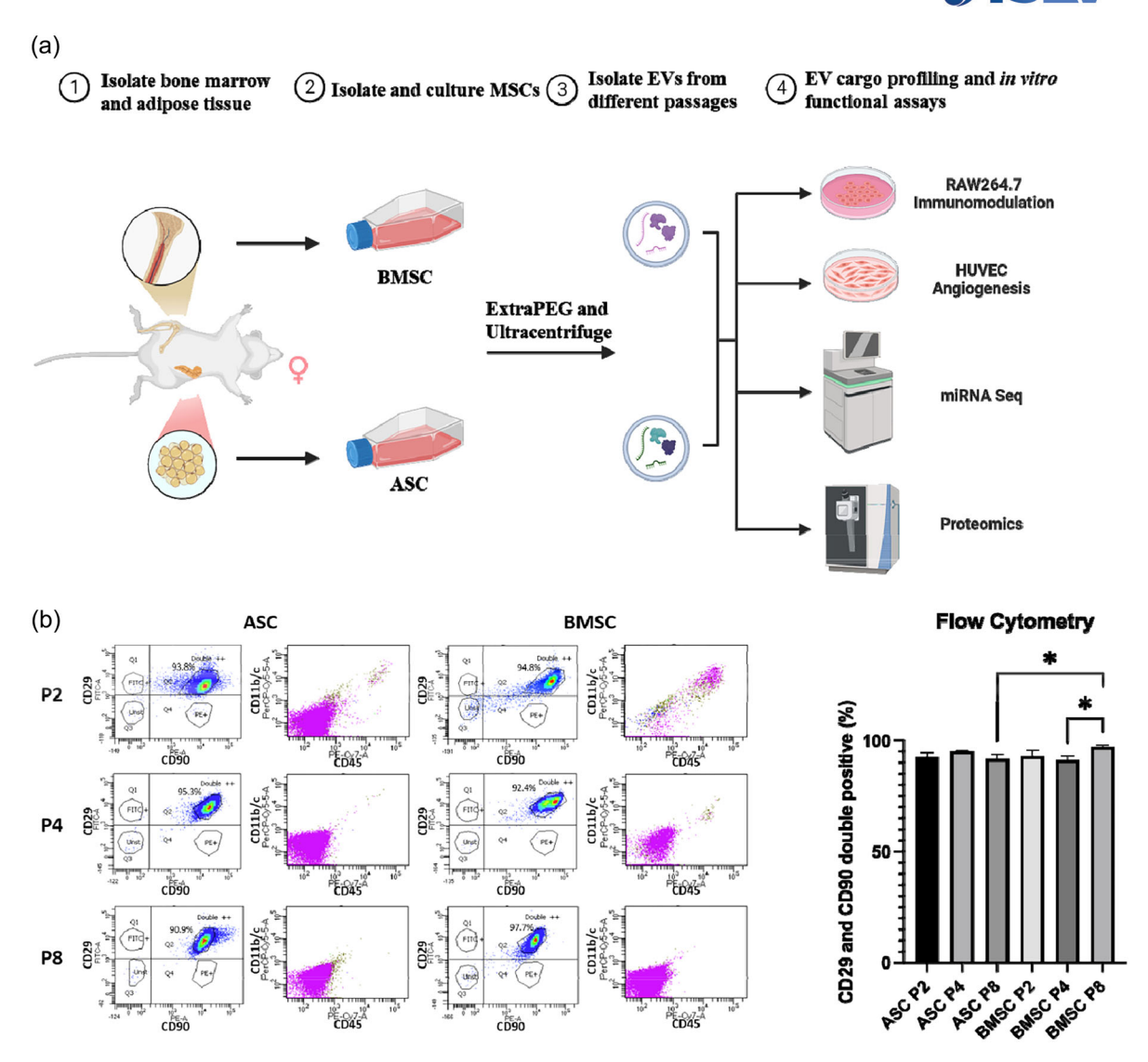


FIGURE 1 (a) Schematic overview of study design, including primary MSC isolation, EV isolation, and in vitro analyses of EVs. (b) Representative plots from flow cytometry analysis (*left*) and statistical analysis (*right*), which confirmed the presence of positive MSC surface markers (FITC-CD29 and PE-CD90) and the absence of negative MSC surface markers (PerCP/Cy5.5-CD11b/c and PE/Cy7-CD45) for primary ASCs and BMSCs at each passage number.

Conditioned culture media from P2, P4, and P8 ASCs and BMCs were collected to isolate EVs and EV sizes and yields were determined by NTA. Both tissue type and passage number had significant effects on EV yield (p = 0.0110 and p = 0.0247, respectively, two-way ANOVA) (Figure 2a, b). Examining the effects of tissue type, pairwise comparisons indicated that BMSCs showed a substantially higher EV yield per cell (97950 \pm 114818 vs. 2276 \pm 1081) than ASC-EVs at P4 (p = 0.0002) (Figure 2b). Although the differences did not reach statistical significance, BMSCs also showed higher EV yields than ASCs at P2, while showing lower yields than ASCs at P8. Focusing on the specific impacts of passaging, EV yield peaked at P4 for BMSCs, while it gradually increased for ASCs up to P8. Significant differences in yield were observed between P2 and P4 for BMSC-EVs ($p \le 0.01$) and P2 and P8 for ASC-EVs ($p \le 0.05$) (Figure 2a).

Although ASC-EVs and BMSC-EVs generally showed similar total protein content per batch across passages (Figure 2c), average protein content normalized to one million EVs was significantly impacted by passage number (p = 0.0129, two-way ANOVA), as it declined with increasing passage number and pairwise comparisons showed a significant difference between P2 and P8 in BMSC-EVs ($p \le 0.05$) (Figure 2d). Passage number did not significantly affect EV size (p = 0.7315); however, P4 and P8 ASC-EVs demonstrated a considerably higher mean diameter than BMSC-EVs ($p \le 0.05$), while P2 EVs were similar in size (Figure 2e). Western blot analysis validated expression of typical positive EV markers (CD9, CD63, HSC70, TSG101) and the absence of negative control markers (Calnexin) on EVs from each tissue source and passage number, although ASC-EVs tended to show slightly lower levels of expression for some markers (Figure 2f). TEM imaging confirmed characteristic cupshaped morphology of EVs at each passage number for both tissue sources (Figure 2g). Taken together, these results indicated

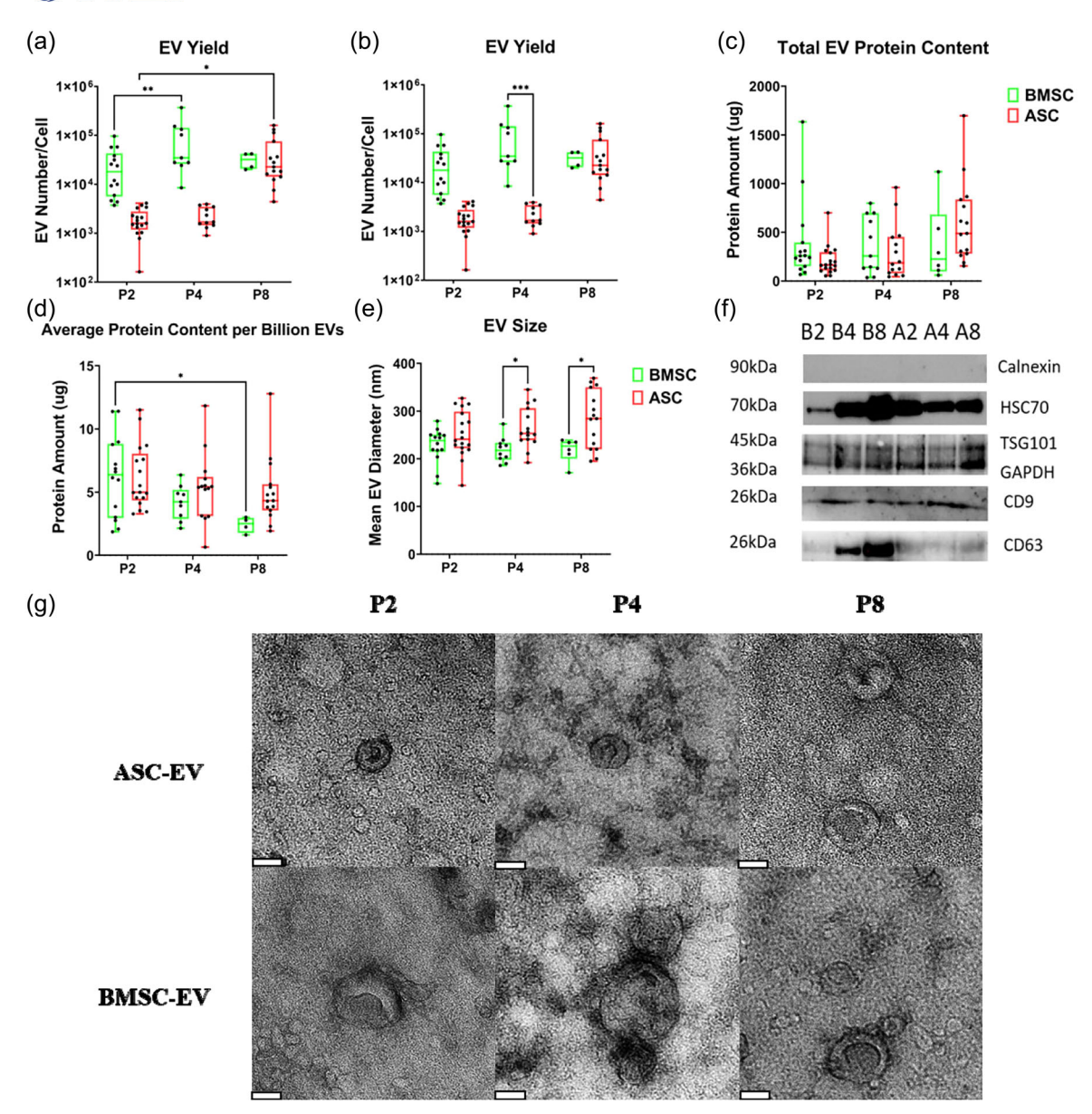


FIGURE 2 Characterization of EV yield (**a**, **b**), total protein content (**c**), average protein content per billion EVs (**d**), EV size (**e**), common EV protein markers (**f**) and EV morphology (**g**) were measured via NTA, BCA assay, western blotting, and TEM for each isolated batch of P2, P4, and P8 ASC-EVs and BMSC-EVs. Data presented as mean \pm SEM (n > 6 biological replicates for P2 and P4 EVs, n = 6 for P8 EVs in EV size and total protein content, n = 4 for P8 EVs in EV yield). Data analysed via two-way ANOVA with Sidak's and Tukey's multiple comparisons. * $p \le 0.05$; ** $p \le 0.01$; *** $p \le 0.001$. Inset white scale bars (**g**) represent 70 μ m.

that EV yield was influenced by both passage number and tissue origin, while EV size was mainly impacted by tissue origin, and normalized protein content was affected by passage number.

3.2 | Proteomics analysis of EV protein cargo

Exosomal proteins have been suggested as the main mechanism of MSC-EV action (Toh et al., 2018). To better understand which proteins underlie the therapeutic potential of MSC-EVs, proteomics analysis was performed on EVs from ASCs and BMSCs at all passages. Principal component analysis (PCA) showed that P2 BMSC-EVs were more heterogeneous in protein content than EVs from the other groups (Figure 3a), reflecting flow cytometry results. The heatmap of differentially expressed proteins (DEPs) displayed distinct profiles for ASC-EVs and BMSC-EVs (Figure 3b). For ASC-EVs, P2 and P4 were more similar in protein profiles than either were to P8. Contrarily, the protein signatures of P4 and P8 EVs were more closely aligned with one another than to P2 in BMSC-EVs. Venn diagrams comparing DEPs with passage number for EVs within the same tissue source showed that

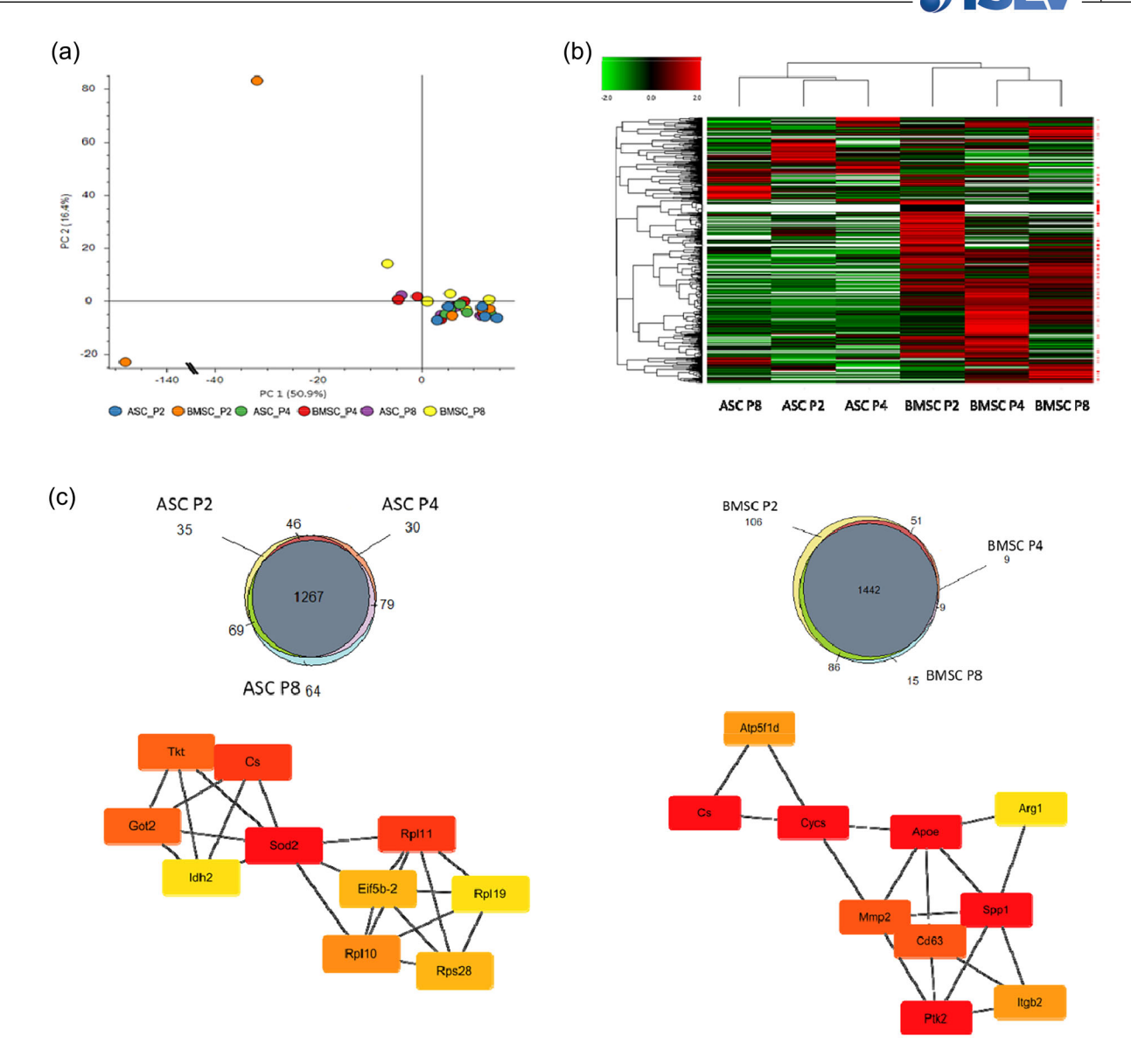


FIGURE 3 Proteomics analysis of differentially expressed proteins (DEP) in EVs from BMSCs and ASCs at P2, P4, and P8. (a) Principal component analysis (PCA) plot. (b) Heatmap of the expression of DEPs between tissue sources and passage numbers. (c) Venn Diagrams comparing DEPs with passage number in ASC-EVs and BMSC-EVs (*top*), and protein-protein interaction maps of the top 10 DEP nodes between P2 and P8 EVs for each MSC type (*bottom*).

BMSC-EVs contained more proteins than ASC-EVs and that the number of DEPs due to passaging was not significant compared to the total shared protein content (Figure 3c *top*). Comparing tissue sources at each passage number, Venn diagrams indicated that BMSC-EVs contained more distinct proteins than ASC-EVs (Figure 4).

GO enrichment analysis of DEPs between early and late passage EVs indicated that the strongest changes related to biological processes were significantly higher expression of tricarboxylic acid (TCA) cycle proteins in P8 compared to P2 ASC-EVs (Table S3), and increased expression of proteins related to positive immune regulation in P2 compared to P8 BMSC-EVs (Table S4). When comparing tissue source differences, ASC-EVs were enriched in proteins that participate in extracellular matrix component regulation, while BMSC-EVs contained significantly higher levels of proteins associated with vesicle biogenesis (Tables S5–S7). Protein-protein interaction analysis of the top 10 DEP nodes between P2 and P8 in ASC-EVs and BMSC-EVs mainly showed different networks between tissue sources, although the common nodes included Citrate Synthase (CS), Cytochrome C, Somatic (CYCS), and Isocitrate Dehydrogenase 2 (IDH2), which represent oxidative metabolism and mitochondrial activities (Figure 3c bottom, Table S8). Comparing DEPs between BMSC-EVs and ASC-EVs at each passage number, Protein Tyrosine Kinase 2 (PTK2) was one of the top 10 DEP nodes at both P2 and P8, which suggests differences in EV capacity to influence cell proliferation, cell migration, and cell survival between the two tissue sources (Sulzmaier et al., 2014) (Figure 4, Table S9). The other DEP nodes at P2 were found to participate in protein synthesis, ribosome biogenesis, and cellular trafficking. The observed differential expression of Integrin Subunit Beta 2 (ITGB2) between ASC-EVs and BMSC-EVs at P4 and P8 implies significantly

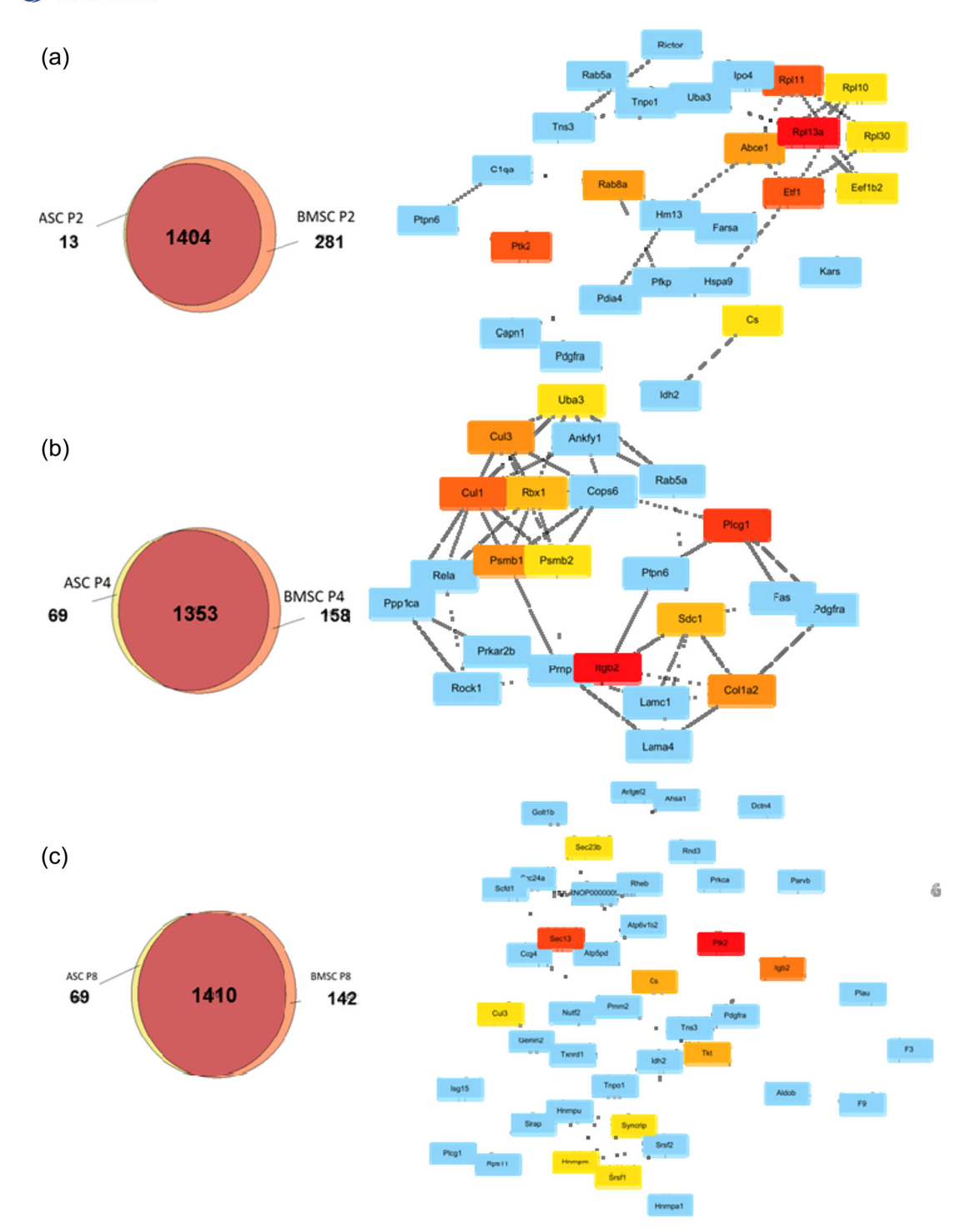


FIGURE 4 Proteomics analysis of DEP in EVs from BMSCs and ASCs at P2 (a), P4 (b), and P8 (c). Venn Diagrams comparing DEPs between BMSC-EVs and ASC-EVs (*left*) and the extended protein-protein interaction maps of the top 10 DEP nodes between BMSC-EVs and ASC-EVs (*right*).

different capacities to promote wound healing and various immune cell functions (Raza et al., 2022). The remaining nine DEP nodes at P4 mainly play roles in ubiquitination and protein degradation, while at P8 they are involved in a wide range of biological processes, such as intracellular transport, mRNA processing and metabolism, and cell adhesion and signalling.

KEGG enrichment analysis of DEPs showed that 2-Oxocarboxylic acid metabolism, a central component of cellular metabolism, was the pathway that had the highest strength score when comparing P2 to P8 in both BMSC-EVs and ASC-EVs, which suggested it to be the key change in EV protein targets after sequential cell subculturing (Tables S10 and S11). Interestingly, when comparing between ASC-EVs and BMSC-EVs at P8, this pathway was also revealed to have the highest strength score, but



not at P2 or P4, reflecting the diverging directions the cells went after a prolonged cell culture period (Tables S12–S14). Pathways involved in Alzheimer's disease and prion disease were also present in the KEGG enrichment analysis of DEPs when comparing P2 to P8 for both tissue sources, indicating that EV therapeutic potential for treatment of neurodegenerative diseases likely changes with passage number. Comparing between ASC-EVs and BMSC-EVs at P2, KEGG analysis showed an enrichment in pathways such as the pentose phosphate pathway and the tricarboxylic acid (TCA) cycle, which are two important elements of cellular metabolism and are critical for the oxidative stress response. Overall, these results indicate that, although a majority of EV proteins were commonly expressed, implying many preserved cargo sorting and functional mechanisms, both tissue source and in vitro passaging impacted the protein cargo of EVs in ways that may contribute to differences in therapeutic capacity.

3.3 | miRNA seq analysis of EV miRNA cargo

In addition to proteins, miRNAs have been identified to play key roles in EV-mediated cellular activities (Pakravan et al., 2017). Although miRNAs only represent a small fraction of exosomal RNA (Nolte-'T Hoen et al., 2012), they are selectively sorted into EVs from parental cells and are shuttled to recipient cells to perform biological functions (Baglio et al., 2015), making them promising candidates for biomarker screening and therapeutic targets. Here, EV miRNAs from both ASCs and BMSCs at different passage numbers were examined via small RNA sequencing with a total of 90 million reads obtained. EV samples from the same passage number and tissue source showed miRNA profile heterogeneity, as indicated by PCA, with P4 ASC-EVs showing the greatest heterogeneity (Figure 5a). Of the 762 miRNAs identified in EV samples, 108 of them were differentially expressed (Figure 5b). Differentially expressed miRNAs (DEMs) from P4 EVs showed similarities to both P2 and P8 EVs in both MSC tissue sources; however, P2 and P8 EVs showed more distinct profiles from one another. Comparing to P2, P8 ASC-EVs displayed 25 DEMs, seven upregulated (e.g., miR-592) and 18 downregulated (e.g., miR-9a-5p) (Figure 6a, Table S15), while P8 BMSC-EVs showed 12 DEMs compared to P2, five upregulated (e.g., miR-298-5p) and seven downregulated (e.g., miR-146a-5p) (Figure 6b, Table S16). The enriched KEGG pathways from the mRNA targets of the DEMs between P2 and P8 EVs in both MSC tissue types included autophagy and microRNAs in cancer (Tables S17 and S18).

More miRNA differences were observed between EV tissue sources at each passage number. Comparing BMSC-EVs with ASC-EVs at P2, 41 total DEMs were discovered, with nine upregulated (e.g., miR-122-5p) and 32 downregulated (e.g., miR-96-5p) (Figure 7a, Table S19). Similarly, when comparing at P4, 29 DEMs were identified, with eight upregulated (e.g., miR-1843a-3p) and 21 downregulated (e.g., miR-211-5p) (Figure 7b, Table S20). At P8, 12 upregulated (e.g., miR-27b-3p) and 15 downregulated (e.g., miR-146a-5p) miRNAs were observed between BMSC-EVs and ASC-EVs, totalling 27 DEMs (Figure 7c, Table S21). Interestingly, microRNAs in cancer still represented one of the most enriched KEGG pathways when comparing tissue source differences at each passage number (Tables S22–S24). Enriched KEGG pathways related to cellular senescence at P4 and apoptosis at P8 suggested that differences in the growth rates of BMSCs and ASCs, which were observed here and in previous studies (Ikegame et al., 2011), were reflected in differences in EV properties relating to in vitro cellular aging. The EV miRNAs differentially expressed between P2 and P4 as well as between P4 and P8 in both tissue sources were also analysed (Tables S25–S27). Surprisingly, no miRNAs were found to be differentially expressed between P4 and P8 in ASC-EVs. Collectively, these results indicate that miRNAs were differentially expressed across different passage numbers and between these two tissues. Interestingly, the differences between miRNAs were generally significantly higher in magnitude than the differences observed in the protein profiling results.

3.4 | EV immunomodulatory capacity

Immunomodulation has been demonstrated by EVs from different MSC sources over a wide range of disease models (Li et al., 2016) and in vitro assays (Song et al., 2017). Here, the effects of EVs derived from ASCs and BMSCs at P2, P4, and P8 on immunomodulatory gene expression were compared in both LPS-stimulated RAW264.7 cells, which modelled acute inflammation, and their unstimulated counterparts. With or without LPS stimulation, EVs more significantly impacted expression of M2-macrophage genes (IL-10, Arg1, TGF β) than M1-macrophage genes (IL-6, NOS2, TNF α) and differences in gene expression largely disappeared by P8 for both EV types (Figure 8, Figure S1). At P2 and P4, BMSC-EVs generally showed a stronger immunomodulatory capacity than ASC-EVs and these effects were dose-dependent. In the presence of LPS stimulation (Figure 8a, Figure S1A), P2 BMSC-EVs significantly increased expression of Arg1 and IL-10 compared to controls and P2 ASC-EVs and enhanced expression of NOS2 compared to controls. Meanwhile, P4 BMSC-EVs significantly upregulated expression of Arg-1 compared to controls and P4 ASC-EVs, yet showed decreased expression of IL-6 compared to P4 ASC-EVs. Interestingly, under basal conditions without LPS stimulation (Figure 8b, Figure S1B), P2 ASC-EVs upregulated expression of Arg-1 compared to controls and P2 BMSC-EVs. By contrast, P4 BMSC-EVs significantly increased expression of Arg-1 compared to controls and P4 ASC-EVs and upregulated expression of IL-10 compared to controls. Changes in gene expression due to EV treatment were generally larger in magnitude under LPS stimulation conditions than when treated with EVs under basal conditions. Statistical analyses showed that effects of EV treatment on almost all genes under LPS stimulation were significantly

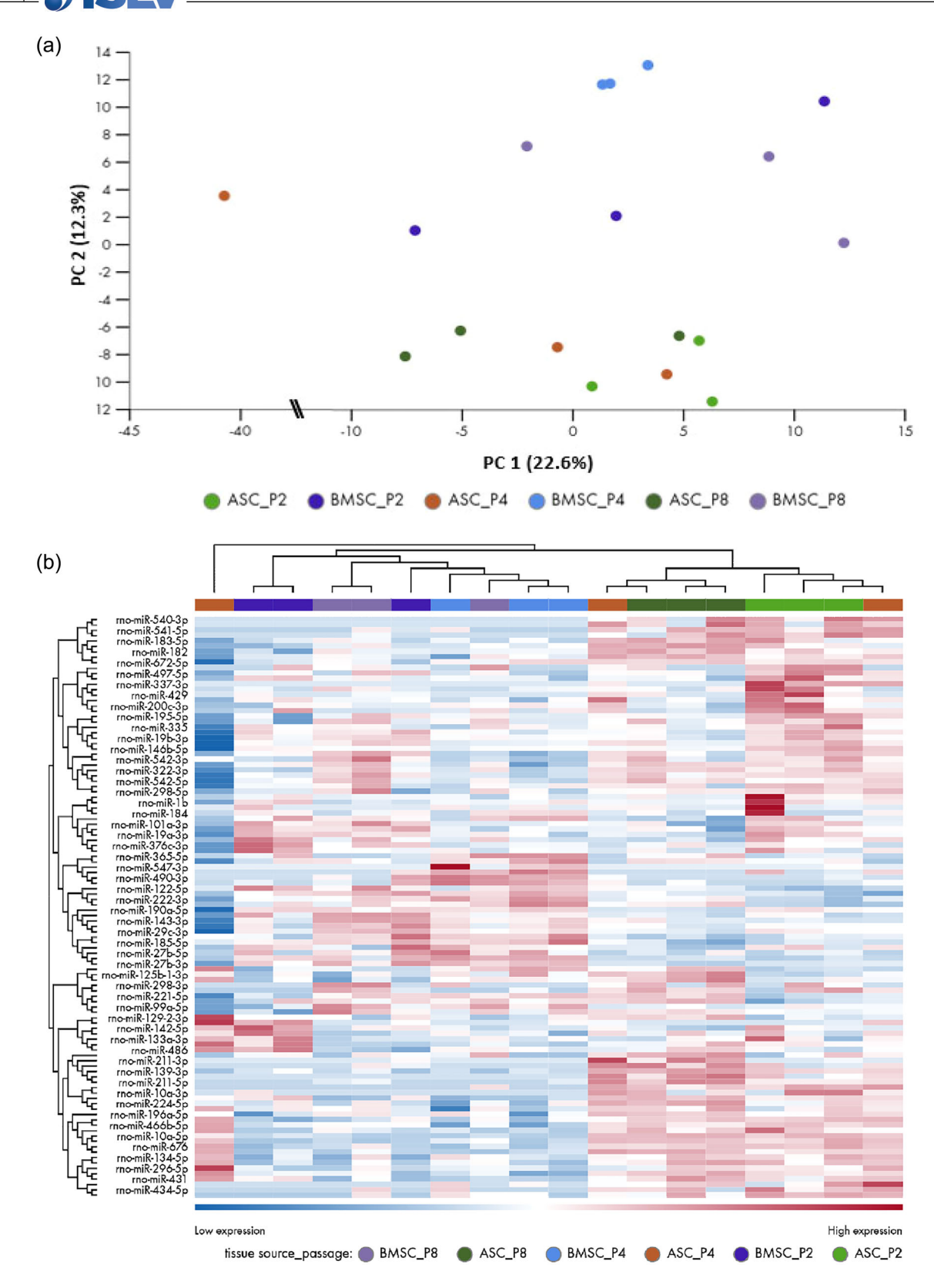


FIGURE 5 miRNA sequencing analysis of differentially expressed miRNAs (DEM) from ASC-EVs and BMSC-EVs at P2, P4, and P8. (a) PCA plot. (b) Heatmap of the expression of DEMs between tissue sources and passage numbers.

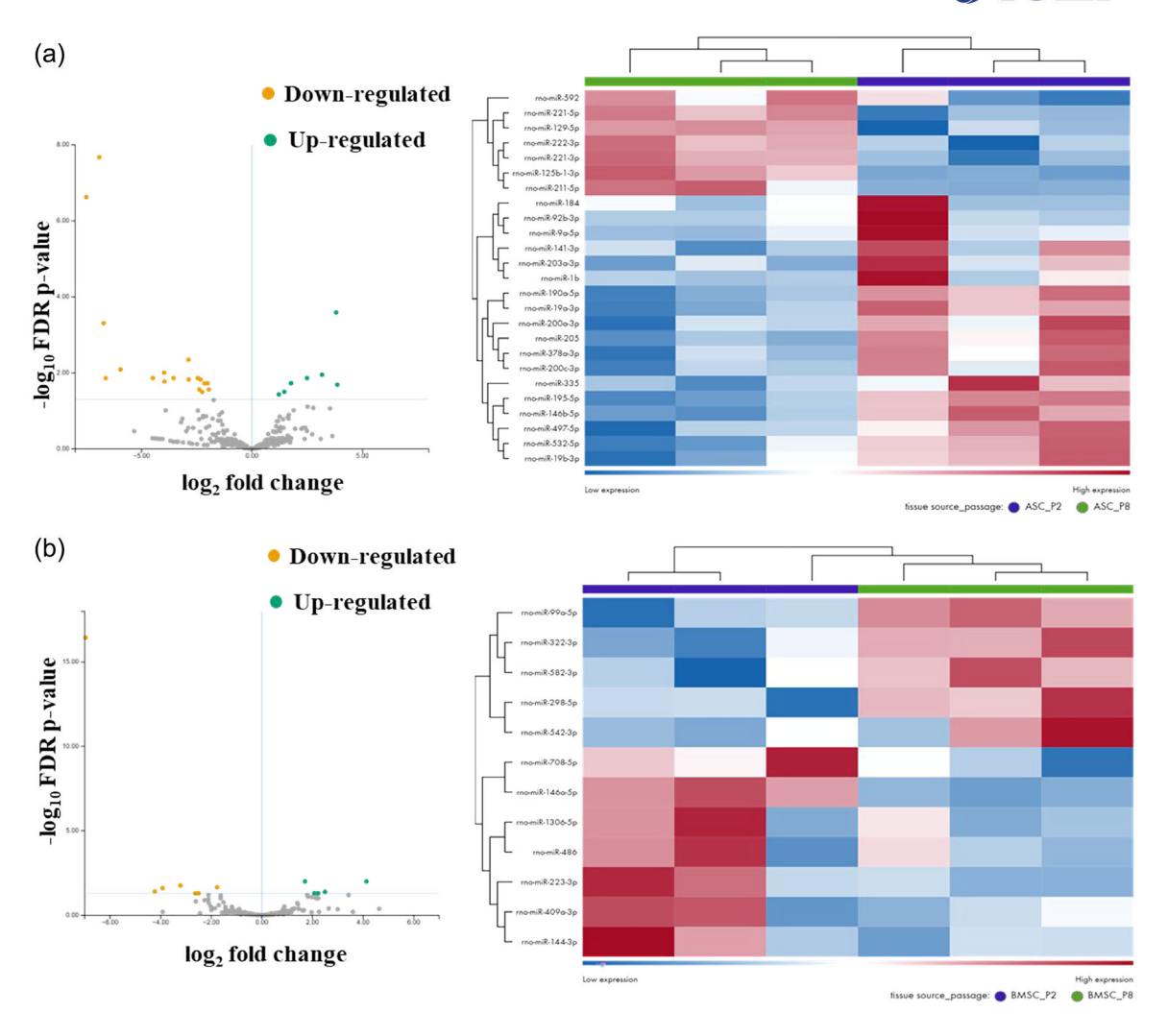


FIGURE 6 miRNA sequencing analysis of DEM comparing between P2 and P8 in ASC-EVs and BMSC-EVs. (a) Volcano plot and heatmap of DEMs between P2 and P8 ASC-EVs. (b) Volcano plot and heatmap of DEMs between P2 and P8 BMSC-EVs.

impacted by passage number, but only expression of Arg-1 and IL-10 were significantly affected by tissue source. Meanwhile, without LPS stimulation, both tissue source and passage number had significant effects on Arg-1, IL-10, and IL-6 expression, while only tissue source impacted NOS2 and only passage number impacted TGF- β expression.

The observed differences in gene expression from LPS-treated cells are not likely due to cell proliferation, as RAW264.7 cells generally showed similar growth patterns over the culture period regardless of EV tissue source or passage number (Figure S2). The observed trends in immunomodulatory gene expression positively correlated with protein abundance differences found in EV proteomics analysis, as shown by multiple immune-related proteins, such as the significantly higher amounts of Argl shown in BMSC-EVs at P2 compared to both P8 BMSC-EVs and to P2 ASC-EVs (Table 1). Overall, earlier passage BMSC-EVs generally showed higher immunomodulatory capacity via upregulation of the expression of anti-inflammatory M2 macrophage genes, with no impacts on RAW264.7 cell proliferation, and these effects were more pronounced under acute inflammation.

3.5 | EV angiogenic capacity

Angiogenesis is critical to tissue repair and regeneration, including cardiac damage repair (Scott et al., 2022), diabetic wound healing (Pomatto et al., 2021), and stroke recovery (Cai et al., 2021). The effects of ASC- and BMSC-derived EVs across passage numbers on in vitro endothelial cell tube formation, proliferation, and angiogenic gene expression were assessed to compare the angiogenic capacity of EVs. HUVECs successfully formed tube structures in every condition evaluated (Figure 9a). EV treatment showed significant effects on total tube length (p = 0.0006), number of nodes (p < 0.0001), number of meshes (p = 0.0041), and number of branches (p < 0.0001), increasing all evaluated angiogenic tube formation parameters. However, passage number

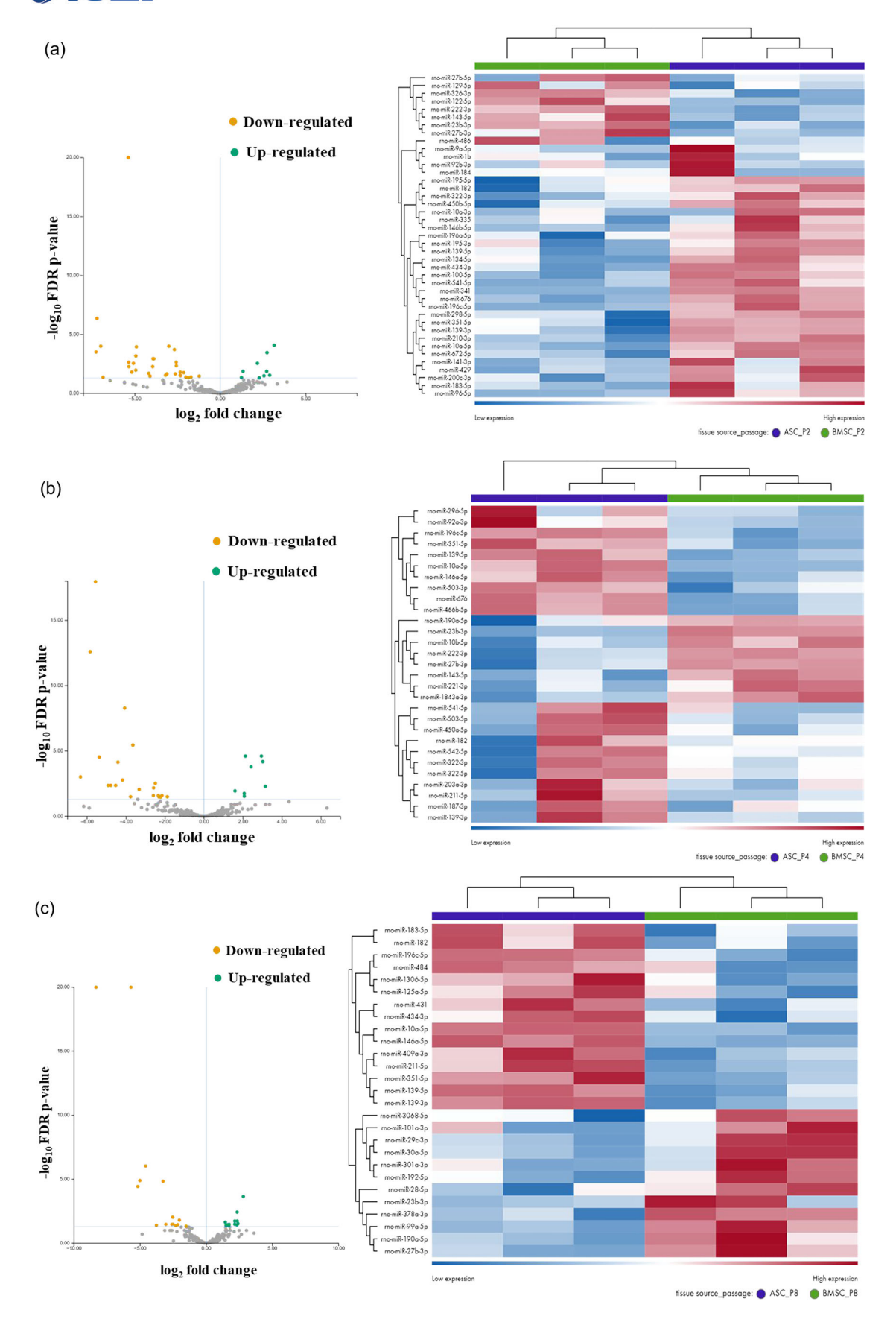


FIGURE 7 Comparison of DEMs between MSC-EV tissue sources at each passage number. Volcano plots (*left*) and heatmaps (*right*) of DEMs between ASC-EVs and BMSC-EVs at P2 (a), P4 (b), and P8 (c).

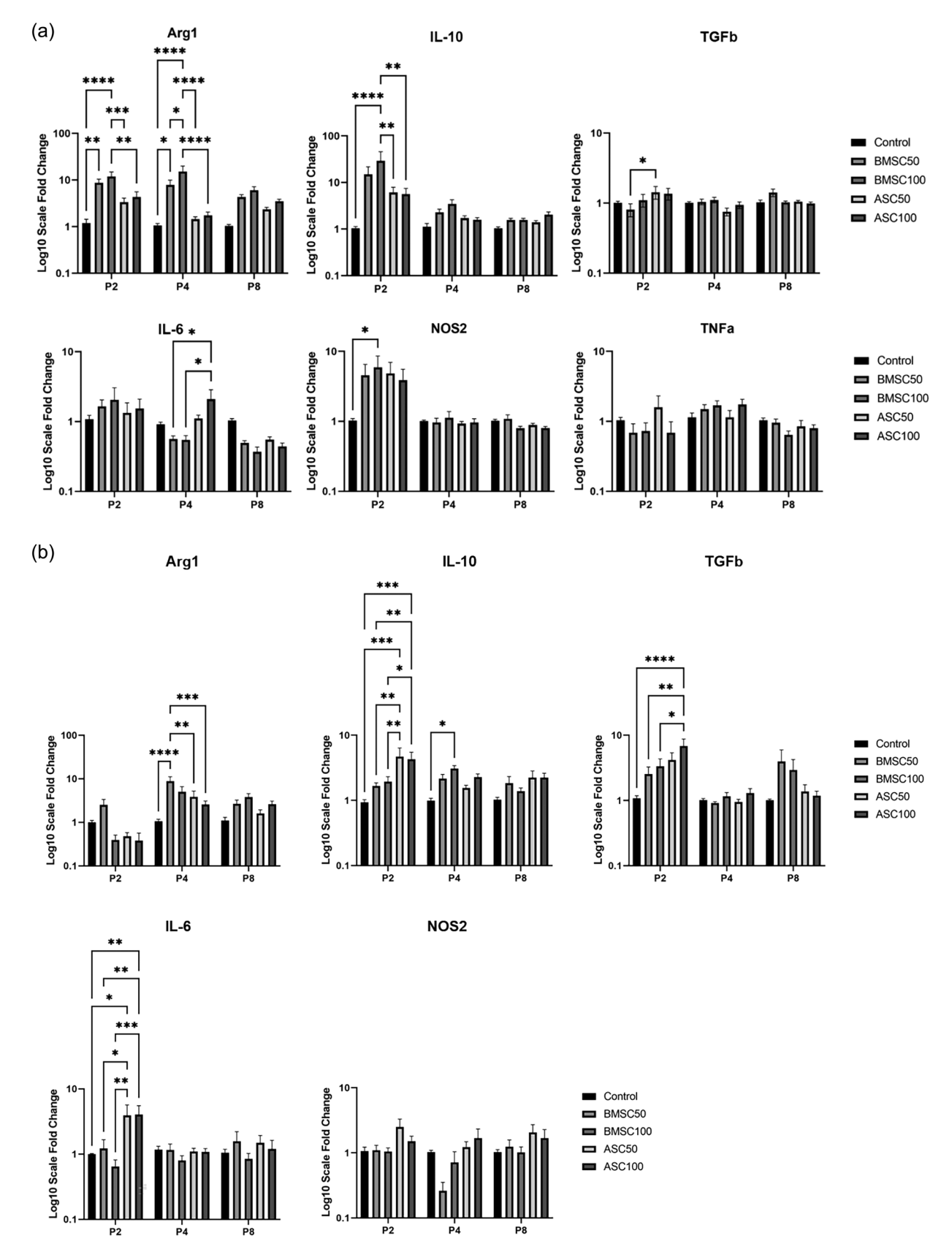


FIGURE 8 Expression levels of M1-type macrophage genes (IL-6, NOS2, TNFa) and M2-type macrophage genes (IL-10, Arg1, TGFb) after 24 h of treatment with P2, P4, and P8 ASC-EVs and BMSC-EVs as evaluated by qRT-PCR at several EV concentrations (50 and 100 μ g/mL) in RAW264.7 cells stimulated with LPS showed significant differences with tissue type and passage number (a). Expression levels of the same set of genes in RAW264.7 cells without LPS stimulation also showed significant differences with MSC-EV tissue type and passage number (b). Data presented as mean \pm SEM (n=4 biological replicates for P2 EVs, n=3 biological replicates for P4 EVs, n=4 biological replicate for P8 EVs). Data analysed via two-way ANOVA with Tukey's multiple comparisons. * $p \le 0.05$; ** $p \le 0.05$; ** $p \le 0.00$; *** $p \le 0.001$; **** $p \le 0.0001$;

TABLE 1 Proteins identified in proteomics analysis related to immunomodulation.

Immunomodulation		
	A2/B2 ratio	adjusted p-value
Argl	0.01	5.73E-17
Stx4	0.01	5.73E-17
Stx11	0.01	5.73E-17
IDH2	0.01	5.73E-17
F3	4.445	0.00306743
	A4/B4 ratio	adjusted p-value
ITGB2	4.046	0.027320375
	A8/B8 ratio	adjusted p-value
IDH2	100	6.96E-17
F3	29.504	8.14E-08
ITGB2	15.197	1.77E-05
	A2/A8 ratio	adjusted p-value
IDH2	0.01	6.66E-17
ITGB2	0.182	0.015816051
	B2/B8 ratio	adjusted p-value
Argl	100	9.20E-17
Il4r	100	9.20E-17
Fcgral	100	9.20E-17
Stx11	100	9.20E-17
IDH2	100	9.20E-17
ITGB2	3.95	0.008752533

only showed significant effects on total length (p = 0.0024) and number of branches (p = 0.0474), with no effects on number of nodes (p = 0.0935) and number of meshes (p = 0.1257) (Figure 9b). At P2, ASC-EVs generally showed significantly higher angiogenic capacity compared to BMSC-EVs in a dose-dependent manner, as supported by increased numbers of nodes, numbers of branches, and numbers of meshes. However, the dose-dependent nature of the effect decreased at P4, while no significant differences were observed at P8. Interestingly, at the 50 μ g/mL dose of BMSC-EVs, P8 induced a significantly higher total tube length than P2. Generally, P2 and P4 ASC-EVs had a greater impact on in vitro angiogenic tube formation, displaying significant increases in most tube formation parameters.

Impedance analysis of HUVEC proliferation indicated that cells treated with BMSC-EVs generally showed a higher proliferation rate over the culture period than those treated with ASC-EVs at each passage number (Figure 9c). When normalized to controls, most of the EV treatment conditions demonstrated a similar effect on cell growth patterns, except for ASC-EVs at P4, which displayed a consistently lower rate of proliferation. The protein abundance differences found in EV proteomics analysis positively correlated with the observed in vitro tube formation trends, with ASC-EVs displaying elevated amounts of multiple angiogenic proteins, such as PDGFRA, compared to BMSC-EVs at each passage number (Table 2).

The expression of several classical angiogenic genes was also analysed after EV treatment in HUVEC cells (Figure 10). Both passage number and EV treatment showed significant impacts on bFGF2 (p=0.0002 and p=0.008, respectively, two-way ANOVA) and TGFb1 expression (p=0.0252 and p<0.0001, respectively, two-way ANOVA). Only EV treatment affected the expression of VEGFA and PDGFB significantly (p=0.0289 and p=0.0153, respectively, two-way ANOVA). Neither of the two factors had significant impacts on HIF1a expression, despite the significant differences found within the P2 group and the ASC group via Tukey's multiple pair-wise comparisons. Overall, ASC-EVs significantly elevated angiogenic gene expression compared to BMSC-EVs at P2; however, this trend was reversed at P4, and fewer differences were observed at P8. P2 ASC-EVs and P4 BMSC-EVs demonstrated superior capacity in increasing angiogenic gene expression compared to other passages and conditions. Angiogenic gene expression changes were generally less than three-fold in magnitude, indicating less dramatic impacts of EVs on angiogenic than immunomodulatory gene expression under the current experimental settings.

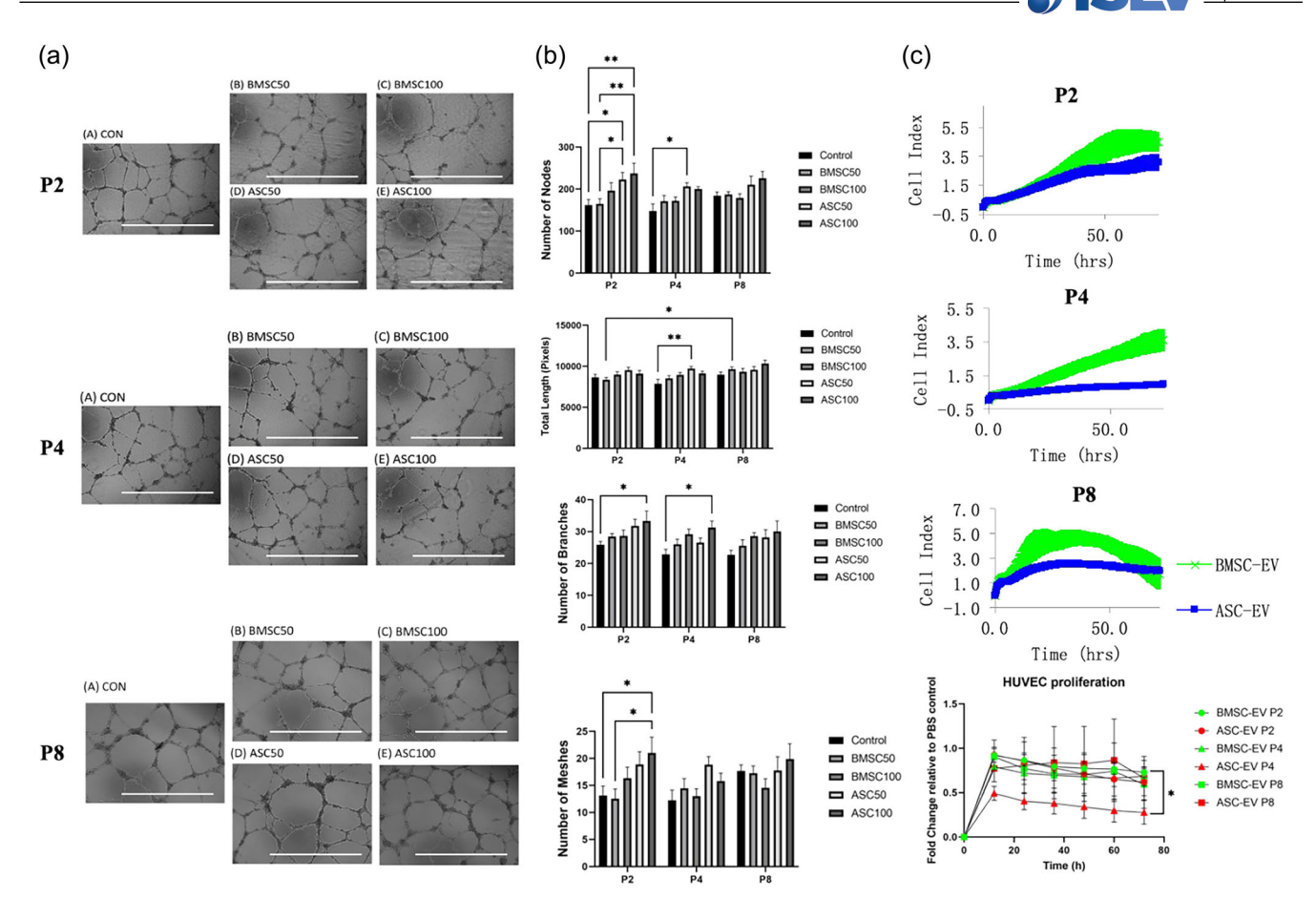


FIGURE 9 HUVEC tube formation assays were performed at several EV concentrations (50 and 100 μ g/mL). (a) Representative microscope images (4 X magnification, scale bar = 1000 μ m) and (b) quantification of representative tube formation parameters of HUVECs treated with P2 EVs, P4 EVs, and P8 EVs. Data presented as mean ± SEM (n = 5 biological replicates for P2 and P4, n = 4 biological replicates for P8). Data analysed via two-way ANOVA with Tukey's multiple comparisons. (c) Proliferation of HUVECs treated with 100 μ g/mL of ASC- and BMSC- EVs from different passage numbers was assessed over 72 h via real-time impedance measurement (n = 3 biological replicates). Representative impedance plots at each passage number (top) and fold-change in cell number normalized to PBS controls at each run (top) Data analysed via two-way ANOVA with Tukey's multiple comparisons. *top ≤ 0.05; *top ≤ 0.01.

3.6 | Effects of EVs on BMSC proliferation

As BMSCs have been widely used in tissue repair and regeneration, the effects of EVs on the proliferation of BMSCs was also evaluated as an indicator of EV capability to initiate robust tissue repair and regeneration processes. BMSC-EVs generally stimulated higher primary BMSC proliferation than ASC-EVs at all passage numbers. Surprisingly, after normalization to controls, treatment with P2 EVs resulted in the lowest fold change in cell number (Figure S3).

4 | DISCUSSION

Several previous studies have compared the effects of tissue sources on the properties of MSC-derived EVs. For example, Pomatto et al. observed that ASC-EVs promoted a significantly higher wound closure rate in vivo and tube formation ratio in vitro, correlating with protein and miRNA cargos related to angiogenesis, while BMSC-EVs induced increased proliferation in keratinocytes and endothelial cells and superior viability in fibroblasts, correlating with cargo molecules associated with proliferation processes (Pomatto et al., 2021). However, most studies to date did not utilize matched donors and many pooled EVs from several MSC passage numbers, leaving the optimal cell source for the development of large-scale clinical MSC-EV therapies unclear. Moreover, while long-term in vitro expansion has been demonstrated to impact MSC proliferative, differentiation, and immunomodulatory capacities, the effects on the properties of MSC-EVs remains underexplored. This study addressed these research gaps by directly comparing EVs from bone marrow and adipose tissues of matched donors and investigating the effects of in vitro expansion on EV cargo composition, as well as in vitro functional properties.

TABLE 2 Proteins identified in proteomics analysis related to angiogenesis.

Angiogenesis		
	A2/B2 ratio	adjusted <i>p</i> -value
Axl	100	5.73E-17
PDGFRA	100	5.73E-17
Jagl	100	5.73E-17
Syndecan-1	14.062	5.94E-05
MMP-2	8.285	0.000422893
Versican	4.593	0.011458736
F3	4.445	0.00306743
NTN4	3.769	0.028737832
PTK2	0.01	5.73E-17
TFPI	0.01	5.73E-17
	A4/B4 ratio	adjusted p-value
NTN4	100	6.64E-17
PDGFRA	100	6.64E-17
Versican	4.612	0.015703852
Syndecan-1	0.01	6.64E-17
	A8/B8 ratio	adjusted p-value
PTK2	100	6.96E-17
NTN4	100	6.96E-17
FZD7	100	6.96E-17
PDGFRA	100	6.96E-17
F3	29.504	8.14E-08
	A2/A8 ratio	adjusted p-value
TFPI	0.01	6.66E-17
PTK2	0.01	6.66E-17
	B2/B8 ratio	adjusted p-value
PTK2	100	9.20E-17
TFPI	100	9.20E-17
NTN4	100	9.20E-17
MMP-2	0.365	0.03772436
Syndecan-1	0.04	2.86E-05
Jagl	0.01	9.20E-17

The significantly higher EV yields observed from BMSCs at P2 and P4 compared to ASCs correlated with proteomics analysis results, which revealed a notable increase (>100-fold change) in proteins related to EV biogenesis and release in BMSC-EVs compared to ASC-EVs, such as Rab35 and CHMP4c at P2, and Rab21 and LAMP2 at P4 (Table 3). However, the total protein content per billion EVs decreased as passage numbers increased for both tissue sources, although this decrease was only statistically significant for BMSC-EVs. Notwithstanding that total protein content is different from the number of proteins identified, proteomics analysis similarly showed that more proteins were identified in P2 BMSC-EVs than in P4 and P8 BMSC-EVs, while the number of proteins remained more consistent across passages for ASC-EVs. Interestingly, although each MSC tissue source showed similar mean EV sizes across passage numbers, the protein content per EV did not correlate with BMSC-EV size. The larger size of ASC-EVs compared to BMSC-EVs at each passage could lead to different internalization mechanisms by recipient cells (Németh et al., 2021), potentially influencing EV therapeutic efficacy. Overall, these results suggest a trade-off between higher protein content, which potentially effects therapeutic capacity, and a larger number of EVs, which enables more efficient production for clinical translation. The maximum EV yields from P4 BMSCs and P8 ASCs could benefit applications requiring production scale-up; however, as these EVs also demonstrated reduced immunomodulation and/or angiogenic capacity in vitro, clinical applications may be limited without additional modifications. Alternatively, P2 BMSC-EVs appear well-suited for

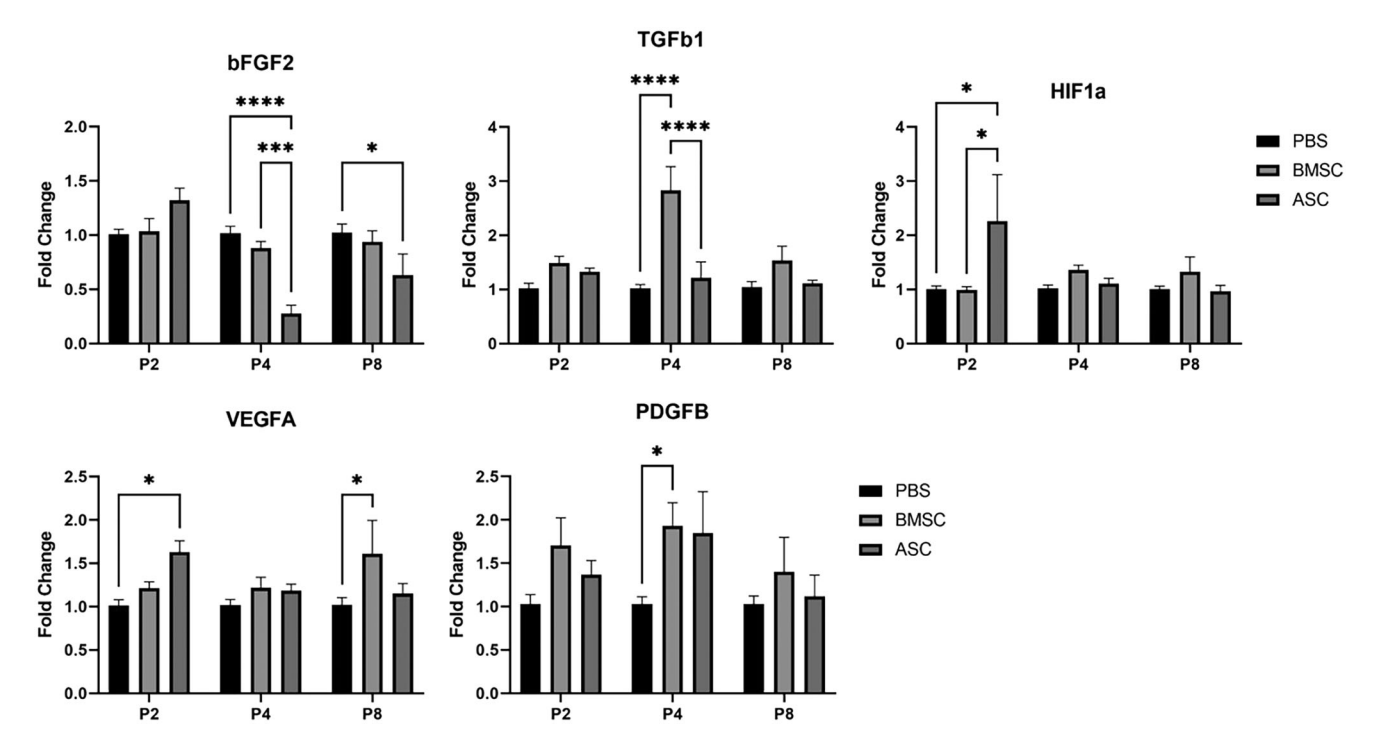


FIGURE 10 Expression levels of angiogenic genes after 24 h of treatment with P2, P4, and P8 ASC-EVs and BMSC-EVs were evaluated by qRT-PCR at a concentration of $100 \,\mu\text{g/mL}$ in HUVEC cells. Data presented as mean \pm SEM (n=3 biological replicate for all EVs). Data analysed via two-way ANOVA with Tukey's multiple comparisons. *p < 0.05; **p < 0.05; **p < 0.00; ***p < 0.00; ****p < 0.00.

TABLE 3 Proteins identified in proteomics analysis related to EV biogenesis/release.

EV biogenesis/release		
	A2/B2 ratio	adjusted <i>p</i> -value
Rab35	0.01	5.73E-17
Rab8a	0.091	0.032706534
Rab5a	0.01	5.73E-17
CHMP4c	0.01	5.73E-17
VPS45	0.01	5.73E-17
Rab34	100	5.73E-17
	A4/B4 ratio	adjusted p-value
Rab21	0.01	6.64E-17
LAMP2	0.01	6.64E-17
Rab5a	0.01	6.64E-17
YKT6	0.01	6.64E-17
	A8/B8	adjusted p-value
Rab27a	0.01	6.96E-17

immunomodulatory applications involving activated macrophages, while P2-P4 ASC-EVs seem most appropriate for angiogenic applications.

Proteomics analyses were performed to investigate how differences in EV protein cargo may be associated with MSC tissue source, in vitro aging due to passaging, and differences in in vitro functional assays. Overall, BMSC-EVs and ASC-EVs showed distinct protein profiles, which is consistent with a previous proteomic study comparing human BMSC-EVs and ASC-EVs (Wang et al., 2020). Similar to our results, hBMSC-EVs contained more unique proteins than hASC-EVs (410 vs. 46), although fewer common proteins were observed at 470. Examining the effects of in vitro aging on EV protein profiles, P2 and P4 were observed to be more closely clustered in ASC-EVs than either to P8, while P4 and P8 were more closely clustered in BMSC-EVs than either to P2. Notably, the greater diversity in protein composition of BMSC-EVs at P2 aligned with the flow cytometry findings, which



demonstrated higher cellular heterogeneity at P2 than at P4 and P8. This suggests a shift in the main subpopulations of BMSCs as the passage number increased that is reflected in the EV protein profile.

As P2 EV protein profiles were most distinct from those of P8 in both MSC tissue types, the differences between these passages were analysed in more detail. The levels of CYCS, which plays a role in mitochondrial activity, were found to be elevated in ASC-EVs and BMSC-EVs at P2 compared to P8, indicating both cell types maintained a higher level of oxidative phosphorylation activity at earlier than at later passage numbers. As glycolysis is often elevated when oxidative phosphorylation is lower to compensate for ATP generation, the elevation of CYCS also implies increased glycolysis in late passage MSCs. Surprisingly, BMSC-EVs exhibited a greater fold change in CYCS than ASC-EVs, which may be attributed to the slower proliferation rate of BMSCs, which required 12 weeks of culture between P2 and P8, compared to 6-weeks for ASCs. The TCA cycle enzymes CS and IDH2, which both play crucial roles in cellular metabolism (Fernie et al., 2004), were increased in ASC-EVs and decreased in BMSC-EVs at P8 when compared to P2, thus suggesting different alterations in energy metabolism and cellular function in ASCs and BMSCs with in vitro expansion. For example, changes in CS, a marker for mitochondrial content (Larsen et al., 2012), imply a shift in metabolic state with passage number, decreasing for BMSCs and increasing for ASCs at P8. Meanwhile, IDH2 generates NADPH thereby facilitating production of nitric oxide (NO) and cellular antioxidants, which are involved in vasodilation (Russell & Richardson, 2022), neurotransmission (Zhu et al., 2021), immune responses, and cellular antioxidant defence (Smolková & Ježek, 2012). Thus, the opposite changes in IDH2 levels could alter the therapeutic efficacy of P8 BMSC-EVs and ASC-EVs in disparate ways.

The most central node in the protein network related to passage number differences in ASC-EVs was superoxide dismutase (SOD2), which was 40-fold higher in P8 than in P2 EVs according to our proteomic analysis, suggesting higher mitochondrial reactive oxygen species (ROS) clearance (Wang et al., 2018) and an antiapoptotic role. Meanwhile, PTK2, also known as focal adhesion kinase (FAK), which is critical in cell attachment to the extracellular matrix (Tapial Martínez et al., 2020), was identified as the central node of passage-related protein differences in BMSC-EVs, with a 100-fold increase at P2 compared to P8, implying decreased cell attachment capacity at late compared to early passage numbers in BMSCs. PTK2 was also significantly higher in P2 BMSC-EVs and P8 ASC-EVs when compared to the EVs of the other MSC type at the same passage number. Given the functions of PTK2 in promoting cell survival, migration, and proliferation, especially in wound healing (Zhang et al., 2022) and cancer metastasis (Sulzmaier et al., 2014), this suggests that P2 BMSC-EVs and P8 ASC-EVs may have higher potential to induce cell survival and migration, which benefits tissue repair.

In our study, ASC-EVs demonstrated a higher capacity to promote HUVEC tube formation compared to BMSC-EVs across all passage numbers, although statistical significance was not reached in all cases. GO analysis suggested that ASC-EVs were enriched in proteins related to: response to wounding at P2; regulating cell adhesion and differentiation and hyaluronan metabolic processes at P4; and, wound healing pathways, vasculature development, and blood vessel development at P8 (Tables S5-S7). The higher levels of specific proteins related to these processes, particularly PDGFRA, could partially explain the superior in vitro angiogenic tube formation capacity demonstrated by ASC-EVs compared to BMSC-EVs, despite the higher abundance of PTK2 in BMSC-EVs at P2 (Table 2). However, GO analysis also indicated that proteins related to cell adhesion and intracellular trafficking signalling pathways were expressed at lower levels in P4 ASC-EVs, which may be associated with the low levels of HUVEC proliferation observed with P4 ASC-EV treatment and the reduced impacts on angiogenic gene expression seen between P2 and P4 ASC-EVs.

Arginase 1 (Arg1), which metabolizes L-arginine to urea and l-ornithine and reduces inflammatory NO production, was found to be significantly higher (>100-fold) in BMSC-EVs than in ASC-EVs at P2, but not at P4 or P8. This may partially explain why the in vitro immunomodulatory effects of BMSC-EVs compared to ASC-EVs were more pronounced at P2 than at P4 and P8, particularly the increased Arg1 expression levels induced in the RAW264.7 cells. GO analysis also indicated that P2 BMSC-EVs contained elevated proteins enriched in the response to interferon-gamma compared to ASC-EVs (Table S5). Interestingly, ITGB2, also known as integrin beta-2 or CD18, which plays a crucial role in leukocyte adhesion and migration during inflammatory responses (Picard et al., 2015), was found to be significantly increased in P4 and P8 ASC-EVs compared to BMSC-EVs at the same passage number, but not in P2 ASC-EVs. This suggests that P4-P8 ASC-EVs may be promising in the treatment of leukocyte adhesion deficiency type 1 (LAD1) disorder (Bouhouche et al., 2022). Meanwhile, focusing solely on the effects of passaging in BMSC-EVs, the significantly higher immunomodulatory effects observed in vitro at P2 compared to P8 were associated with remarkably higher EV content of immune response proteins, such as Arg1, Itgb2, Il4r, Stx11, and Fcgr1a (Table 1). GO analysis also showed the enrichment of biological processes such as positive regulation of myeloid leukocyte mediated immunity and lymphocyte mediated immunity in the differentially expressed proteins between P2 and P8 in BMSC-EVs (Table S4). By contrast, ITGB2 and IDH2 were observed at lower levels in P2 compared to P8 ASC-EVs.

Comparative small RNA sequencing studies have been performed previously on human BMSC-EVs and ASC-EVs (Baglio et al., 2015); however, here the profiling results include a focus on miRNA biological functions. The significant differentially expressed common miRNAs between BMSC-EVs and ASC-EVs at each passage number, such as miR-10a-5p, miR-196c-5p, miR-139-3p, miR-139-5p, miR-182, and miR-27b-3p, all participate in regulating cell proliferation and differentiation. Notably, the top differentially expressed miRNAs between MSC sources at each passage number have been shown to be associated with angiogenesis, such as: miR-96-5p (Desjarlais et al., 2020) and miR-9a-5p (Yi & Gao, 2019) at P2; miR-211-5p (Pan et al., 2019) and

miR-10a-5p (Zhang et al., 2021) at P4; and, miR-196c-5p (Zhi et al., 2016) at P8 (TablesS19-S21). Meanwhile, miR-146a-5p, which plays key roles in the regulation of the immune system and is often upregulated in response to pro-inflammatory stimuli (Taganov et al., 2006), such as LPS, was significantly downregulated in P8 compared to P2 BMSC-EVs as well as in late passage (P4 and P8) BMSC-EVs compared to ASC-EVs; suggesting that late passage BMSC-EVs may have a diminished capacity to modulate recipient cell responses to pro-inflammatory stimuli, as was observed in our LPS-stimulated RAW264.7 cell qRT-PCR results. Interestingly, miR-146a-5p has also been found to reduce production of angiogenic factors, such as VEGF, in endothelial cells (Ye & Steinle, 2017), which may explain the observed increase in VEGFA expression in HUVECs treated with P8 BMSC-EVs but not at P2 or P4. The target mRNAs of the significantly upregulated miRNAs found in P2 compared to P8 ASC-EVs were enriched in signalling pathways related to angiogenesis involved in wound healing and vascular endothelial growth factor signalling, which may have contributed to the ASC-EV HUVEC tube formation capacity observed across different passages.

Although our proteomics and miRNA seq analyses identified several key EV cargo molecules that were differentially expressed due to in vitro expansion as well as between ASC-EVs and BMSC-EVs, these results need to be confirmed through further Western blotting, ELISA, and qRT-PCR analyses. More importantly, it remains somewhat unclear whether the identified candidate proteins and miRNAs are the main mechanisms underlying the observed in vitro differences in angiogenic, immunomodulatory, and proliferation-inducing capacities between ASC-EVs and BMSC-EVs and/or between early and late passage MSC-EVs. For example, in addition to increased Arg-1 protein levels, other upregulated EV cargo molecules in P2 BMSC-EVs compared to ASC-EVs that could contribute to the observed increase in immunomodulatory capacity include miR-129-5p and miR-27b-3p, although these miRNAs only showed around a 7-fold increase (Table S19). Overexpression of miR-129-5p in MSC-EVs has been shown to suppress M1 macrophage polarization in a rat model of intervertebral disc degeneration (Cui & Zhang, 2021), while miR-27b-3p can suppress macrophage colony-stimulating factor-1 (Liu et al., 2022), which regulates macrophage survival, proliferation, and differentiation. Meanwhile, the increased angiogenic capacity of ASC-EVs compared to BMSC-EVs at P2 and P4 may be due to increases in EV cargo content of PDGFRA, miR-96-5p (Desjarlais et al., 2020), miR-9a-5p (Yi & Gao, 2019), and/or miR-10-a-5p (Zhang et al., May, 2021) or another entirely different mechanism. Future experiments employing antibody and siRNA inhibitors will be necessary to further interrogate these candidate pathways and molecules.

Additional research is necessary to confirm that the observed effects of MSC tissue source and in vitro expansion on EV properties in this study employing rat cells are reflected in human ASC-EVs and BMSC-EVs. By focusing on the comparison of EVs derived from ASCs and BMSCs, the results of this study are translatable to the development of both allogenic EV therapies, which better enable production scale-up for clinical translation, and autologous EV therapies, which minimize adverse immune reactions and have been shown to be more therapeutically effective than their allogenic counterparts in preclinical wound healing models (Lu et al., 2019). Future studies are also needed to determine whether observed differences in EV properties are also associated with alterations in EV internalization efficiencies or pathways. For example, the differences observed here in EV size between late passage ASC-EVs and BMSC-EVs could impact internalization, as the higher curvature of smaller vesicles could lead to more efficient endocytosis via alternative pathways (Chen et al., 2016). Differences in EV membrane protein and lipid composition have been shown to impact the selectivity and efficiency of target cell internalization as well as affecting systemic clearance by macrophages (Zhang et al., 2022). Thus, as this study only examined EV miRNA and total protein cargo, future work will more thoroughly characterize EV surface molecules and analyse other cargo molecules, such as mRNA and lipids.

A major limitation of this study was the restricted nature of the in vitro assessments of MSC-EV immunomodulatory and angiogenic capacity. Immunomodulatory studies will be expanded in the future to include T-cell proliferation and exhaustion assays, while results of gene expression analyses in EV-treated macrophages and endothelial cells will be confirmed through protein analyses. More importantly, in vivo studies are necessary to validate whether the in vitro differences in MSC-EV angiogenic and immunomodulatory properties due to tissue source and in vitro passaging are clinically relevant. Future studies employing wound and bone healing models will be conducted to confirm whether the increased angiogenic potential of early passage ASC-EVs and the enhanced immunomodulatory capacity of early passage BMSC-EVs observed here in vitro translate to the more complex in vivo environment.

Results from this study suggest that future work employing genetic manipulation tools or changes in the culture environment should be explored to increase the EV yield of early passage MSC-EVs and/or increase the therapeutic potential of late passage EVs to better enable clinical translation. For example, Chen et al. found that oncogenic immortalization preserved the capacity of human ESC-derived MSCs to generate therapeutic exosomes (Chen et al., 2011). Alternatively, specific EV targeting and/or drug-loading strategies could be explored to increase the therapeutic potential of later passage MSC-EVs. Using a combinatorial strategy, Kang et al. showed that conjugation of human peripheral blood-derived sEVs with a cardiac-targeting peptide and further loading with NADPH Oxidase 4 (NOX4) siRNA (siNOX4) resulted in significantly increased EV heart-targeting ability and therapeutic efficacy in a murine model of impaired cardiac function (Kang et al., 2023). Thus, further enhancement of MSC-EV yield or therapeutic capacity could be investigated through modifications such as gene editing, surface conjugation, and/or drug loading to further optimize MSC-EV therapies for a specific disease or tissue regeneration application.

5 | CONCLUSIONS

Our study demonstrated that both tissue source and passage number affected MSC-EV yield, protein content, miRNA content, and in vitro angiogenic and immunomodulatory capacity. BMSCs displayed higher EV yields than ASCs at earlier passages, while ASC-EVs were larger than BMSC-EVs at later passages. BMSC-EVs induced higher HUVEC and BMSC proliferation throughout different passages and demonstrated stronger immunomodulatory capacity in LPS-stimulated macrophages at earlier passages. By contrast, ASC-EVs demonstrated stronger immunomodulatory effects in the absence of LPS-stimulation at P2 and a higher angiogenic capacity across passages. Differences in EV miRNA and protein cargos played important roles in immunomodulation and angiogenesis. Changes in EV protein cargos due to passaging reflected changes in cellular metabolism with in vitro expansion. Overall, the results of this study suggest that the optimal MSC source for production of clinical EV therapies for a specific application should be chosen carefully based on their EV properties; for example, ASC-EVs appear to be better for angiogenesis, while BMSC-EVs seem to be better for acute inflammation, and EVs should be derived from early passage (P2 to P4) MSCs in most cases.

AUTHOR CONTRIBUTIONS

Yuan Liu: Conceptualization (equal); data curation (lead); formal analysis (lead); investigation (lead); methodology (equal); visualization (lead); writing—original draft (lead); writing—review and editing (supporting). Li Sun: Methodology (supporting); resources (supporting); writing—review and editing (supporting). Yan Li: Funding acquisition (supporting); project administration (supporting); supervision (supporting); writing—review and editing (supporting). Christina Holmes: Conceptualization (equal); data curation (supporting); formal analysis (supporting); funding acquisition (lead); methodology (equal); project administration (lead); supervision (lead); visualization (supporting); writing—original draft (supporting); writing—review and editing (lead).

ACKNOWLEDGEMENTS

The authors would like to thank the translational science laboratory and flow cytometry laboratory in the College of Medicine and the molecular cloning facility in the Department of Biological Sciences at Florida State University for assistance in proteomics, flow cytometry, and miRNA sequencing analyses, particularly Dr. Rakesh Singh, Dr. Yanming Yang, Beth Alexander, Amber Brown, and Cynthia Vied. The authors would like to thank Dr. Michelle Arbetman for kindly allowing use of her qRT-PCR machine. The authors would like to thank Leanne Duke from the College of Medicine for assistance in lab maintenance and training in NTA, ultracentrifugation, and TEM. This work is supported by an FSU start up fund and is partially supported by the National Institutes of Health (USA) under Award Number R16GM151369 (to C.H.) and R01NS125016 (to Y.L.). The content is solely the responsibility of the authors and does not necessarily represent the official views of the National Institutes of Health.

CONFLICT OF INTEREST STATEMENT

The authors declared no conflict of interests.

DATA AVAILABILITY STATEMENT

The data that support the findings of this study are available from the corresponding author upon reasonable request.

ORCID

Li Sun https://orcid.org/0000-0001-8228-7487 *Christina Holmes* https://orcid.org/0000-0003-0736-0503

REFERENCES

Bagge, J., Berg, L. C., Janes, J., & Macleod, J. N. (2022). Donor age effects on in vitro chondrogenic and osteogenic differentiation performance of equine bone marrow- and adipose tissue-derived mesenchymal stromal cells. BMC Veterinary Research, 18(1), 388. https://doi.org/10.1186/s12917-022-03475-2

Baglio, S. R., Rooijers, K., Koppers-Lalic, D., Verweij, F. J., Pérez Lanzón, M., Zini, N., Naaijkens, B., Perut, F., Niessen, H. W., Baldini, N., & Pegtel, D. M. (2015). Human bone marrow- and adipose-mesenchymal stem cells secrete exosomes enriched in distinctive miRNA and tRNA species. *Stem Cell Research Therapy*, 6(1), 127, https://doi.org/10.1186/s13287-015-0116

Bian, S., Zhang, L., Duan, L., Wang, X., Min, Y., & Yu, H. (2014). Extracellular vesicles derived from human bone marrow mesenchymal stem cells promote angiogenesis in a rat myocardial infarction model. *Journal of Molecular Medicine*, 92(4), 387–397. https://doi.org/10.1007/S00109-013-1110-5/FIGURES/6

Bouhouche, A., Tabache, Y., Askander, O., Charoute, H., Mesnaoui, N., Belayachi, L., El Hafidi, N., Hardizi, H., El Fahime, E., Erreimi, N., Barakat, A., Khattab, M., Seghrouchni, F., & El Hassani, A. (2022). Novel ITGB2 mutation is responsible for a severe form of leucocyte adhesion deficiency type 1. *BioMed Research International*, 2022, 1–8. https://doi.org/10.1155/2022/1141280

Cai, G., Cai, G., Zhou, H., Zhuang, Z., Liu, K., Pei, S., Wang, Y., Wang, H., Wang, X., Xu, S., Cui, C., Sun, M., Guo, S., Jia, K., Wang, X., & Zhang, D. (2021). Mesenchymal stem cell-derived exosome miR-542-3p suppresses inflammation and prevents cerebral infarction. Stem Cell Research and Therapy, 12(1), 2. https://doi.org/10.1186/s13287-020-02030-w



- Carpentier, G., Berndt, S., Ferratge, S., Rasband, W., Cuendet, M., Uzan, G., & Albanese, P. (2020). Angiogenesis Analyzer for ImageJ A comparative morphometric analysis of 'Endothelial Tube Formation Assay' and 'Fibrin Bead Assay'. *Scientific Reports*, 10(1), 11568. https://doi.org/10.1038/s41598-020-67289-8
- Chen, L., Xiao, S., Zhu, H., Wang, L., & Liang, H. (2016). Shape-dependent internalization kinetics of nanoparticles by membranes. Soft Matter, 12(9), 2632–2641. https://doi.org/10.1039/c5sm01869b
- Chen, T. S., Arslan, F., Yin, Y., Tan, S. S., Lai, R. C., Choo, A. B. H., Padmanabhan, J., Lee, C. N., De Kleijn, D. P., & Lim, S. K. (2011). Enabling a robust scalable manufacturing process for therapeutic exosomes through oncogenic immortalization of human ESC-derived MSCs. *Journal of Translational Medicine*, 9, 47. https://doi.org/10.1186/1479-5876-9-47
- Cui, S., & Zhang, L. (2021). microRNA-129-5p shuttled by mesenchymal stem cell-derived extracellular vesicles alleviates intervertebral disc degeneration via blockade of LRG1-mediated p38 MAPK activation. *Journal of Tissue Engineering*, 12, 204173142110216. https://doi.org/10.1177/20417314211021679
- Dehghani, L., Khojasteh, A., Soleimani, M., Oraee-Yazdani, S., Keshel, S., Saadatnia, M., Saboori, M., Zali, A., Hashemi, S., & Soleimani, R. (2022). Safety of intraparenchymal injection of allogenic placenta mesenchymal stem cells derived exosome in patients undergoing decompressive craniectomy following malignant middle cerebral artery infarct, a pilot randomized clinical trial. *International Journal of Preventive Medicine*, *13*(1), 7. https://doi.org/10.4103/IJPVM. IJPVM 441 21
- Desjarlais, M., Wirth, M., Rivera, J. C., Lahaie, I., Dabouz, R., Omri, S., Ruknudin, P., Borras, C., & Chemtob, S. (2020). MicroRNA-96 promotes vascular repair in oxygen-induced retinopathy—A novel uncovered vasoprotective function. Frontiers in Pharmacology, 11, 13. https://doi.org/10.3389/fphar.2020.00013
- Dong, F., Harvey, J., Finan, A., Weber, K., Agarwal, U., & Penn, M. S. (2012). Myocardial CXCR4 expression is required for mesenchymal stem cell mediated repair following acute myocardial infarction. *Circulation*, 126(3), 314–324. https://doi.org/10.1161/CIRCULATIONAHA.111.082453
- Fernández-Santos, M. E., García-Arranz, M., Andreu, E. J., García-Hernández, A. M., López-Parra, M., Villarón, E., Sepúlveda, P., Fernández-Avilés, F., García-Olmo, D., Prosper, F., Sánchez-Guijo, F., Moraleda, J. M., & Zapata, A. G. (2022). Optimization of mesenchymal stromal cell (MSC) manufacturing processes for a better therapeutic outcome. Frontiers in Immunology, 13, 918565. https://doi.org/10.3389/fimmu.2022.918565
- Fernie, A. R., Carrari, F., & Sweetlove, L. J. (2004). Respiratory metabolism: Glycolysis, the TCA cycle and mitochondrial electron transport. Current Opinion in Plant Biology, 7(3), 254–261. https://doi.org/10.1016/j.pbi.2004.03.007
- Gong, P., Zhang, W., He, Y., Wang, J., Li, S., Chen, S., Ye, Q., & Li, M. (2021). Classification and characteristics of mesenchymal stem cells and its potential therapeutic mechanisms and applications against ischemic stroke. Stem Cells International, 2021, 1–13. https://doi.org/10.1155/2021/2602871
- Gudleviciene, Z., Kundrotas, G., Liudkeviciene, R., Rascon, J., & Jurga, M. (2015). Quick and effective method of bone marrow mesenchymal stem cell extraction. Open Medicine (Poland), 10(1), 44–49. https://doi.org/10.1515/med-2015-0008
- Guillamat-Prats, R. (2021). The role of MSC in wound healing, scarring and regeneration. Cells, 10(7), 1729. https://doi.org/10.3390/cells10071729
- Hoang, D. H., Nguyen, T. D., Nguyen, H.-P., Nguyen, X.-H., Do, P. T. X., Dang, V. D., Dam, P. T. M., Bui, H. T. H., Trinh, M. Q., Vu, D. M., Hoang, N. T. M., Thanh, L. N., & Than, U. T. T. (2020). Differential wound healing capacity of mesenchymal stem cell-derived exosomes originated from bone marrow, adipose tissue and umbilical cord under serum- and xeno-free condition. Frontiers in Molecular Biosciences, 7, 119. https://doi.org/10.3389/fmolb.2020.00119
- Huang, Q., Huang, Y., & Liu, J. (2021). Mesenchymal stem cells: An excellent candidate for the treatment of diabetes mellitus. *International Journal of Endocrinology*, 2021, 1–11. https://doi.org/10.1155/2021/9938658
- Ikegame, Y., Yamashita, K., Hayashi, S.-I., Mizuno, H., Tawada, M., You, F., Yamada, K., Tanaka, Y., Egashira, Y., Nakashima, S., Yoshimura, S.-I., & Iwama, T. (2011). Comparison of mesenchymal stem cells from adipose tissue and bone marrow for ischemic stroke therapy. *Cytotherapy*, *13*(6), 675–685. https://doi.org/10.3109/14653249.2010.549122
- Kadri, N., Amu, S., Iacobaeus, E., Boberg, E., & Le Blanc, K. (2023). Current perspectives on mesenchymal stromal cell therapy for graft versus host disease. Cellular and Molecular Immunology, 20(6), 613–625. https://doi.org/10.1038/s41423-023-01022-z
- Kang, J.-Y., Mun, D., Chun, Y., Park, D.-S., Kim, H., Yun, N., & Joung, B. (2023). Engineered small extracellular vesicle-mediated NOX4 siRNA delivery for targeted therapy of cardiac hypertrophy. *Journal of Extracellular Vesicles*, 12(10), e12371. https://doi.org/10.1002/jev2.12371 <./bi>
- Kim, H., Zhao, Q., Barreda, H., Kaur, G., Hai, B., Choi, J. M., Jung, S. Y., Liu, F., & Lee, R. H. (2021). Identification of molecules responsible for therapeutic effects of extracellular vesicles produced from iPSC-derived MSCs on Sjo gren's Syndrome. *Aging Disease*, 12(6), 1409. https://doi.org/10.14336/AD.2021.0621
- Larsen, S., Nielsen, J., Hansen, C. N., Nielsen, L. B., Wibrand, F., Stride, N., Schroder, H. D., Boushel, R., Helge, J. W., Dela, F., & Hey-Mogensen, M. (2012). Biomarkers of mitochondrial content in skeletal muscle of healthy young human subjects. *Journal of Physiology*, 590(14), 3349–3360. https://doi.org/10.1113/jphysiol.2012.230185
- Lässer, C., Eldh, M., & Lötvall, J. (2012). Isolation and characterization of RNA-containing exosomes. *Journal of Visualized Experiments*, 00(59), e3037. https://doi.org/10.3791/3037
- Li, J., Pan, Y., Yang, J., Wang, J., Jiang, Q., Dou, H., & Hou, Y. (2022). Tumor necrosis factor-α-primed mesenchymal stem cell-derived exosomes promote M2 macrophage polarization via Galectin-1 and modify intrauterine adhesion on a novel murine model. *Frontiers in Immunology*, 13, 945234. https://doi.org/10.3389/fimmu.2022.945234
- Li, X., Liu, L., Yang, J., Yu, Y., Chai, J., Wang, L., Ma, L., & Yin, H. (2016). Exosome derived from human umbilical cord mesenchymal stem cell mediates MiR-181c attenuating burn-induced excessive inflammation. eBioMedicine, 8, 72–82. https://doi.org/10.1016/j.ebiom.2016.04.030
- Lin, F., Chen, W., Zhou, J., Zhu, J., Yao, Q., Feng, B., Feng, X., Shi, X., Pan, Q., Yu, J., Li, L., & Cao, H. (2022). Mesenchymal stem cells protect against ferroptosis via exosome-mediated stabilization of SLC7A11 in acute liver injury. Cell Death & Disease, 13(3), 271. https://doi.org/10.1038/s41419-022-04708-w
- Liu, W., Rong, Y., Wang, J., Zhou, Z., Ge, X., Ji, C., Jiang, D., Gong, F., Li, L., Chen, J., Zhao, S., Kong, F., Gu, C., Fan, J., & Cai, W. (2020). Exosome-shuttled miR-216a-5p from hypoxic preconditioned mesenchymal stem cells repair traumatic spinal cord injury by shifting microglial M1/M2 polarization. *Journal of Neuroinflammation*, 17(1), 47. https://doi.org/10.1186/s12974-020-1726-7
- Liu, Y., & Holmes, C. (2021). Tissue regeneration capacity of extracellular vesicles isolated from bone marrow-derived and adipose-derived mesenchymal stromal/stem cells. Frontiers in Cell and Developmental Biology, 9, 648098. https://doi.org/10.3389/fcell.2021.648098
- Liu, Y., Zhang, Z., Wang, B., Dong, Y., Zhao, C., Zhao, Y., Zhang, L., Liu, X., Guo, J., Chen, Y., Zhou, J., Yang, T., Wang, Y., Liu, H., & Wang, S. (2022). Inflammation-stimulated MSC-derived small extracellular vesicle miR-27b-3p regulates macrophages by targeting CSF-1 to promote temporomandibular joint condylar regeneration. Small, 18(16), e2107354. https://doi.org/10.1002/smll.202107354
- Lu, M., Peng, L., Ming, X., Wang, X., Cui, A., Li, Y., Wang, X., Meng, D., Sun, N., Xiang, M., & Chen, S. (2019). Enhanced wound healing promotion by immune response-free monkey autologous iPSCs and exosomes vs. their allogeneic counterparts. eBioMedicine, 42, 443, https://doi.org/10.1016/J.EBIOM.2019.03.011
- Matas, J., García, C., Poblete, D., Vernal, R., Ortloff, A., Luque-Campos, N., Hidalgo, Y., Cuenca, J., Infante, C., Cadiz, M. I., Khoury, M., Luz-Crawford, P., & Espinoza, F. (2024). A phase I dose-escalation clinical trial to assess the safety and efficacy of umbilical cord-derived mesenchymal stromal cells in knee osteoarthritis. Stem Cells Translational Medicine, 13(3), 193. https://doi.org/10.1093/STCLTM/SZAD088



- Matas, J., Orrego, M., Amenabar, D., Infante, C., Tapia-Limonchi, R., Cadiz, M. I., Alcayaga-Miranda, F., González, P. L., Muse, E., Khoury, M., Figueroa, F. E., & Espinoza, F. (2019). Umbilical cord-derived mesenchymal stromal cells (MSCs) for knee osteoarthritis: Repeated MSC dosing is superior to a single MSC dose and to hyaluronic acid in a controlled randomized phase I/II trial. Stem Cells Translational Medicine, 8(3), 215–224. https://doi.org/10.1002/sctm.18-0053
- Maumus, M., Jorgensen, C., & Noël, D. (2013). Mesenchymal stem cells in regenerative medicine applied to rheumatic diseases: Role of secretome and exosomes. Biochimie, 95(12), 2229–2234. https://doi.org/10.1016/j.biochi.2013.04.017
- Nagelkerke, A., Ojansivu, M., Van Der Koog, L., Whittaker, T. E., Cunnane, E. M., Silva, A. M., Dekker, N., & Stevens, M. M. (2021). Extracellular vesicles for tissue repair and regeneration: Evidence, challenges and opportunities. Advanced Drug Delivery Reviews, 175, 113775. https://doi.org/10.1016/j.addr.2021.04.013
- Németh, K., Varga, Z., Lenzinger, D., Visnovitz, T., Koncz, A., Hegedűs, N., Kittel, Á., Máthé, D., Szigeti, K., Lőrincz, P., O'neill, C., Dwyer, R., Liu, Z., Buzás, E. I., & Tamási, V. (2021). Extracellular vesicle release and uptake by the liver under normo- and hyperlipidemia. *Cellular and Molecular Life Sciences*, 78(23). 7589–7604. https://doi.org/10.1007/s00018-021-03969-6
- Nimma, R., Kalvala, A. K., Patel, N., Surapaneni, S. K., Sun, L., Singh, R., Nottingham, E., Bagde, A., Kommineni, N., Arthur, P., Nathani, A., Meckes, D. G., & Singh, M. (2022). Combined transcriptomic and proteomic profiling to unravel osimertinib, CARP-1 functional mimetic (CFM 4.17) formulation and telmisartan combo treatment in NSCLC tumor xenografts. *Pharmaceutics*, 14(6), 1156. https://doi.org/10.3390/pharmaceutics14061156
- Nolte-'T Hoen, E. N. M., Buermans, H. P. J., Waasdorp, M., Stoorvogel, W., Wauben, M. H. M., & 'T Hoen, P. A. C. (2012). Deep sequencing of RNA from immune cell-derived vesicles uncovers the selective incorporation of small non-coding RNA biotypes with potential regulatory functions. *Nucleic Acids Reseastch*, 40(18), 9272–9285. https://doi.org/10.1093/nar/gks658
- Pakravan, K., Babashah, S., Sadeghizadeh, M., Mowla, S. J., Mossahebi-Mohammadi, M., Ataei, F., Dana, N., & Javan, M. (2017). MicroRNA-100 shuttled by mesenchymal stem cell-derived exosomes suppresses in vitro angiogenesis through modulating the mTOR/HIF-1α/VEGF signaling axis in breast cancer cells. *Cellular Oncology*, 40(5), 457–470. https://doi.org/10.1007/s13402-017-0335-7
- Pan, J., Wang, X., Li, D., Li, J., & Jiang, Z. (2019). MSCs inhibits the angiogenesis of HUVECs through the miR-211/Prox1 pathway. *Journal of Biochemistry*, 166(1), 107–113. https://doi.org/10.1093/jb/mvz038
- Picard, C., Al-Herz, W., Bousfiha, A., Casanova, J.-L., Chatila, T., Conley, M. E., Cunningham-Rundles, C., Etzioni, A., Holland, S. M., Klein, C., Nonoyama, S., Ochs, H. D., Oksenhendler, E., Puck, J. M., Sullivan, K. E., Tang, M. L. K., Franco, J. L., & Gaspar, H. B. (2015). Primary immunodeficiency diseases: An update on the classification from the International Union of Immunological Societies Expert Committee for Primary Immunodeficiency. *Journal of Clinical Immunology*, 35(8), 696. https://doi.org/10.1007/s10875-015-0201-1
- Pomatto, M., Gai, C., Negro, F., Cedrino, M., Grange, C., Ceccotti, E., Togliatto, G., Collino, F., Tapparo, M., Figliolini, F., Lopatina, T., Brizzi, M. F., & Camussi, G. (2021). Differential therapeutic effect of extracellular vesicles derived by bone marrow and adipose mesenchymal stem cells on wound healing of diabetic ulcers and correlation to their cargoes. *International Journal of Molecular Sciences*, 22(8), 3851. https://doi.org/10.3390/ijms22083851
- Raposio, E., Simonacci, F., & Perrotta, R. E. (2017). Adipose-derived stem cells: Comparison between two methods of isolation for clinical applications. *Annals of Medicine and Surgery*, 20, 87–91. https://doi.org/10.1016/j.amsu.2017.07.018
- Raza, R., Khalid, Z., Zaman, A., Jafar, S., Anwar, M. Z., Hassan, S. W., Iqbal, M., Rashid, S., Ahmad, W., & Raza, S. I. (2022). Sequence variants in the ITGB2 gene underlying leukocyte adhesion deficiency Type-1 in four consanguineous families. *Gene Reports*, 29, 101699. https://doi.org/10.1016/j.genrep.2022.101699
- Rider, M. A., Hurwitz, S. N., & Meckes, D. G. (2016). ExtraPEG: A polyethylene glycol-based method for enrichment of extracellular vesicles. *Scientific Reports*, 6, 23978. https://doi.org/10.1038/srep23978
- Russell, T. M., & Richardson, D. R. (2022). Glutathione-S-transferases as potential targets for modulation of nitric oxide-mediated vasodilation. *Biomolecules*, 12(9), 1292. https://doi.org/10.3390/biom12091292
- Scott, S. R., March, K. L., Wang, I.-W., Singh, K., Liu, J., Turrentine, M., Sen, C. K., & Wang, M. (2022). Bone marrow- or adipose-mesenchymal stromal cell secretome preserves myocardial transcriptome profile and ameliorates cardiac damage following ex vivo cold storage. *Journal of Molecular and Cellular Cardiology*, 164, 1–12. https://doi.org/10.1016/j.yjmcc.2021.11.002
- Shi, M.-M., Yang, Q.-Y., Monsel, A., Yan, J.-Y., Dai, C.-X., Zhao, J.-Y., Shi, G.-C., Zhou, M., Zhu, X.-M., Li, S.-K., Li, P., Wang, J., Li, M., Lei, J.-G., Xu, D., Zhu, Y.-G., & Qu, J.-M. (2021). Preclinical efficacy and clinical safety of clinical-grade nebulized allogenic adipose mesenchymal stromal cells-derived extracellular vesicles. e12134. https://doi.org/10.1002/jev2.12134
- Shin, J. Y., Kim, D.-Y., Lee, J., Shin, Y. J., Kim, Y. S., & Lee, P. H. (2022). Priming mesenchymal stem cells with α-synuclein enhances neuroprotective properties through induction of autophagy in Parkinsonian models. Stem Cell Research Therapy, 13(1), 483. https://doi.org/10.1186/s13287-022-03139-w
- Smolková, K., & Ježek, P. (2012). The role of mitochondrial NADPH-dependent isocitrate dehydrogenase in cancer cells. *International Journal of Cell Biology*, 2012, 1–12. https://doi.org/10.1155/2012/273947
- Song, Y., Dou, H., Li, X., Zhao, X., Li, Y., Liu, D., Ji, J., Liu, F., Ding, L., Ni, Y., & Hou, Y. (2017). Exosomal miR-146a contributes to the enhanced therapeutic efficacy of interleukin-1β-primed mesenchymal stem cells against sepsis. Stem Cells, 35(5), 1208–1221. https://doi.org/10.1002/stem.2564
- Sulzmaier, F. J., Jean, C., & Schlaepfer, D. D. (2014). FAK in cancer: Mechanistic findings and clinical applications. *Nature Reviews Cancer*, 14(9), 598–610. https://doi.org/10.1038/nrc3792
- Taganov, K. D., Boldin, M. P., Chang, K.-J., & Baltimore, D. (2006). NF-κB-dependent induction of microRNA miR-146, an inhibitor targeted to signaling proteins of innate immune responses. *PNAS*, 103(33), 12481–12486. https://doi.org/10.1073/pnas.0605298103
- Tapial Martínez, P., López Navajas, P., & Lietha, D. (2020). FAK structure and regulation by membrane interactions and force in focal adhesions. *Biomolecules*, 10(2), 179. https://doi.org/10.3390/biom10020179
- Toh, W. S., Lai, R. C., Zhang, B., & Lim, S. K. (2018). MSC exosome works through a protein-based mechanism of action. *Biochemical Society Transactions*, 46(4), 843–853. https://doi.org/10.1042/BST20180079
- Wang, L., Gu, Z., Zhao, X., Yang, N., Wang, F., Deng, A., Zhao, S., Luo, L., Wei, H., Guan, L., Gao, Z., Li, Y., Wang, L., Liu, D., & Gao, C. (2016). Extracellular vesicles released from human umbilical cord-derived mesenchymal stromal cells prevent life-threatening acute graft-versus-host disease in a mouse model of allogeneic hematopoietic stem cell transplantation. Stem Cells and Development, 25(24), 1874–1883. https://doi.org/10.1089/scd.2016.0107
- Wang, Y., Branicky, R., Noë, A., & Hekimi, S. (2018). Superoxide dismutases: Dual roles in controlling ROS damage and regulating ROS signaling. *Journal of Cell Biology*, 217(6), 1915–1928. https://doi.org/10.1083/jcb.201708007
- Wang, Z.-G., He, Z.-Y., Liang, S., Yang, Q., Cheng, P., & Chen, A.-M. (2020). Comprehensive proteomic analysis of exosomes derived from human bone marrow, adipose tissue, and umbilical cord mesenchymal stem cells. Stem Cell Research Therapy, 11(1), 511. https://doi.org/10.1186/s13287-020-02032-8
- Xu, H., Wang, Z., Liu, L., Zhang, B., & Li, B. (2020). Exosomes derived from adipose tissue, bone marrow, and umbilical cord blood for cardioprotection after myocardial infarction. *Journal of Cellular Biochemistry*, 121(3), 2089–2102. https://doi.org/10.1002/jcb.27399
- Ye, E. A., & Steinle, J. J. (2017). miR-146a suppresses STAT3/VEGF pathways and reduces apoptosis through IL-6 signaling in primary human retinal microvascular endothelial cells in high glucose conditions. Vision Research, 139, 15–22. https://doi.org/10.1016/j.visres.2017.03.009



- Yi, J., & Gao, Z.-F. (2019). MicroRNA-9-5p promotes angiogenesis but inhibits apoptosis and inflammation of high glucose-induced injury in human umbilical vascular endothelial cells by targeting CXCR4. *International Journal of Biological Macromolecules*, 130, 1–9. https://doi.org/10.1016/j.ijbiomac.2019.02.003
- Zhang, J., Brown, A., Johnson, B., Diebold, D., Asano, K., Marriott, G., & Lu, B. (2022). Genetically engineered extracellular vesicles harboring transmembrane scaffolds exhibit differences in their size, expression levels of specific surface markers and cell-uptake. *Pharmaceutics*, 14(12), 2564. https://doi.org/10.3390/pharmaceutics14122564
- Zhang, Q., Shi, L., He, H., Liu, X., Huang, Y., Xu, D., Yao, M., Zhang, N., Guo, Y., Lu, Y., Li, H., Zhou, J., Tan, J., Xing, M., & Luo, G. (2022). Down-regulating scar formation by microneedles directly via a mechanical communication pathway. ACS Nano, 16(7), 10163–10178. https://doi.org/10.1021/acsnano.1c11016
- Zhang, X., Wang, Y., Wang, X., Zou, B., Mei, J., Peng, X., & Wu, Z. (2021). Extracellular vesicles-encapsulated microRNA-10a-5p shed from cancer-associated fibroblast facilitates cervical squamous cell carcinoma cell angiogenesis and tumorigenicity via Hedgehog signaling pathway. *Cancer Gene Therapy*, 28(5), 529–542. https://doi.org/10.1038/S41417-020-00238-9
- Zhang, Z., Huang, S., Wu, S., Qi, J., Li, W., Liu, S., Cong, Y., Chen, H., Lu, L., Shi, S., Wang, D., Chen, W., & Sun, L. (2019). Clearance of apoptotic cells by mesenchymal stem cells contributes to immunosuppression via PGE2. eBioMedicine, 45, 341–350. https://doi.org/10.1016/j.ebiom.2019.06.016
- Zhao, L., Yu, J., Wang, J., Li, H., Che, J., & Cao, B. (2017). Isolation and identification of miRNAs in exosomes derived from serum of colon cancer patients. Journal of Cancer, 8(7), 1145–1152. https://doi.org/10.7150/jca.18026
- Zhi, F., Xue, L., Shao, N., Deng, D., Kang, X., Xu, Y., Wang, R., Yang, Y., & Xia, Y. (2016). δ-opioid receptor activation and microRNA expression in the rat heart under prolonged hypoxia. *Cellular Physiology and Biochemistry*, 39(3), 1118–1128. https://doi.org/10.1159/000447815
- Zhu, H.-Y., Hong, F.-F., & Yang, S.-L. (2021). The roles of nitric oxide synthase/nitric oxide pathway in the pathology of vascular dementia and related therapeutic approaches. *International Journal of Molecular Sciences*, 22(9), 4540. https://doi.org/10.3390/ijms22094540
- Zhu, Y.-G., Shi, M.-M., Monsel, A., Dai, C.-X., Dong, X., Shen, H., Li, S. K., Chang, J., Xu, C.-L., Li, P., Wang, J., Shen, M.-P., Ren, C.-J., Chen, D. C., & Qu, J.-M. (2022). Nebulized exosomes derived from allogenic adipose tissue mesenchymal stromal cells in patients with severe COVID-19: A pilot study. Stem Cell Research Therapy, 13(1), 220, https://doi.org/10.1186/s13287-022-02900-5
- Zhu, Y., Wang, Y., Zhao, B., Niu, X., Hu, B., Li, Q., Zhang, J., Ding, J., Chen, Y., & Wang, Y. (2017). Comparison of exosomes secreted by induced pluripotent stem cell-derived mesenchymal stem cells and synovial membrane-derived mesenchymal stem cells for the treatment of osteoarthritis. Stem Cell Research & Therapy, 8(1), 64. https://doi.org/10.1186/s13287-017-0510-9
- Zou, J., Yang, W., Cui, W., Li, C., Ma, C., Ji, X., Hong, J., Qu, Z., Chen, J., Liu, A., & Wu, H. (2023). Therapeutic potential and mechanisms of mesenchymal stem cell-derived exosomes as bioactive materials in tendon–bone healing. *Journal of Nanobiotechnology*, 21(1), 14. https://doi.org/10.1186/s12951-023-01778-6

SUPPORTING INFORMATION

Additional supporting information can be found online in the Supporting Information section at the end of this article.

How to cite this article: Liu, Y., Sun, L., Li, Y., & Holmes, C. (2024). Mesenchymal stromal/stem cell tissue source and in vitro expansion impact extracellular vesicle protein and miRNA compositions as well as angiogenic and immunomodulatory capacities. *Journal of Extracellular Vesicles*, 13, e12472. https://doi.org/10.1002/jev2.12472